Studies of aerodynamically induced vibrations on the P-3Cmaritime surveillance aircraft and proposed vibration reducing measures

Øyvind Andreassen, Carl Erik Wasberg, Anders Helgeland, Murat Tutkun, Jan Charles Kielland, Bjørn Anders Pettersson Reif, Øistein Lundberg and Atle Skaugen

Norwegian Defence Research Establishment (FFI)

31 January 2013

FFI-rapport 2013/00245

385301

P: ISBN 978-82-464-2203-9
E: ISBN 978-82-464-2204-6

Keywords

CFD-simuleringer

Vibrasjonsanalyse

Aerodynamikk

Fairing

P-3C

Approved by

Bjørn Anders Petterson Reif	Project Manager
Jan Ivar Botnan	Director

English summary

After installation of a radome on the P-3C aircraft, vibrations occur in flight that were not present earlier. The vibrations are specially noticeable at high airspeeds. The cause of the vibrations is confirmed to be random or partly oscillatory aerodynamic forces caused by the radome and acting at the aft part of the aircraft. The vibrations are experienced to be unpleasant for the crew and there is a risk that they can lead to formation of cracks and fatigue of main framework or reinforcing structures of the airplane. To reduce the vibrations to a safe and comfortable level, we have to understand their cause. FFI has occasionally been engaged in this problem through in-flight vibration measurements, through the design of aerodynamic counter measures that we call “fairings” and by carrying out computational fluid dynamics (CFD) simulations to study the topology and consequences of the strongly turbulent wake downstream the radome and the forces acting at the aft part of the fuselage.

The radome is shaped as a hemisphere attached to a cylinder with same radius as the hemisphere. It extends beyond the fuselage and alters the airflow at the aft part of the airplane. A horseshoe vortex and a massive turbulent wake is formed. Both CFD analysis, wind tunnel measurements and vibration measurements during flight have been used to identify the nature of the problem. Test flights were carried through last summer. For the vibration measurements, 15 accelerometers were mounted at carefully selected points at the aircraft frame. Three test flights were undertaken. One with the radome dismounted which we call clean aircraft, one with the radome attached and one with the radome and fairing attached.

We have designed several fairings formed like a wedge with a fillet and a pair of vortex generators. The purpose has been to alter the airflow of the radome wake in a way that will reduce vibrations. The attempt has been to weaken the horseshoe vortex and the intensity of the turbulent wake and to move the vortices and wake away from the fuselage. CFD simulations have indicated that the effect of the fairing is as expected and the footprint of the radome wake that touches the fuselage is more narrow which results in a weakening of the aerodynamic forces and torques acting on the fuselage.

0.1 Results

The vibrations were strongest in the flight regime of high airspeed. The strongest vibrations were registered in the aft part of the boom. The vibrations increase with distance from center of gravity (CG). Lowest levels of the vibrations were observed with clean airplane. The strongest vibrations were observed with the radome without fairing. The effect of the fairing is as expected. The measured vibrations are reduced during nearly all flight conditions compared to airplane with radome. The fairing produces counter-rotating vortices that weaken the radome generated horseshoe vortex and wake. The vortex generator that we have tested has a moderate impact. A more active vortex generator could reduce vibrations even more.

Sammendrag

Etter installasjon av en ny radom på P-3C maritimt overvåkningsfly forekommer vibrasjoner under flyvning som ikke var der tidligere. Vibrasjonene er spesielt merkbare ved høye “air speeds”. Opphavet til vibrasjonene er bekreftet å være stokastiske og tildels oscillerende aerodynamiske krefter forårsaket av radomen som virker på bakkroppen på flyet. Vibrasjonene er ubehagelige for bemanningen og det er risiko for at sprekker og tretthetsskader vil opptre i flyets bærende strukturer. For å kunne redusere vibrasjonene til et sikkert og komfortabelt nivå må vi forstå grunnen til at de opptrer. FFI har ved flere anledninger blitt engasjert i dette problemkomplekset gjennom vibrasjonsmålinger under flyvning, gjennom design av aerodynamiske motmidler som vi kaller “fairings” og ved å utføre (CFD - computational fluid dynamics) simuleringer for å studere topologi og konsekvenser av den sterkt turbulente luftstrømmen nedstrøms i forhold til radomen og kreftene som virker på flyets bakkropp.

Radomen er formet som en halvkule festet på en sylinder med samme radius som kula. Radomen stikker ut av skroget og påvirker luftstrømmen bakover. En hesteskovirvel og et massivt turbulent kjølvann dannes. Både CFD analyse, vindtunnel-eksperimenter og vibrasjonsmålinger under flyvning har blitt benyttet til å identifisere årsaken til problemet. Sommeren 2012 ble 15 akselerometere montert på spesielt uvalgte punkter på flyet. Tre testflyvninger ble gjennomført. En med radomen fjernet fra flyet som vi kaller “clean aircraft”, en med radomen og en med radom og “fairing”.

Vi har designet flere “fairinger” formet som en kile med avrunding og et par virvelgeneratorer. Formålet har vært å endre luftstrømmen i radomkjølvannet slik at påvirkningen på flyet blir svakere. Vi har forsøkt å svekke hesteskovirvelen og turbulensintensiteten i kjølvannet samtidig som vi har forsøkt å trekke virvlene ut fra flyskroget. CFD-simuleringene har indikert at effekten av fairingen er som forventet og at fotavtrykket av kjølvannet mot flyskroget er svakere og smalere enn for radom uten fairing. Dette reduserer de aerodynamiske kreftene som påvirker skroget.

0.2 Resultater

Vibrasjonene var sterkest i flyvningsregimet med høy hastighet, og vibrasjonene økte med avstand fra tyngdepunktet (CG), dvs de sterkeste vibrasjonene ble registrert bakerst i bommen.
Det er alltid vibrasjoner i et fly. Sommerens testkampanje viste at det laveste nivået på vibrasjoner ble observert for “clean aircraft”. De sterkeste vibrasjonene ble observert med radom uten fairing. Effekten av fairingen var som forventet. Vibrasjonene ble redusert under nesten alle flyforhold sammenlignet med radome uten fairing.
Fairingen genererer motroterende virvler som demper virvler og kjølvann forårsaket av radomen. Virvelgeneratoren som vi har testet har en moderat virkning. En mer aktiv virvelgenerator kan potensielt redusere vibrasjonene ytterligere.

Contents

1 Introduction

Under flight, the P-3C aircraft as any aircraft exhibits a wide spectrum of natural vibrational modes. Some of these modes accumulate more energy than others and one typically find several maxima in the power-spectra. For the P-3C aircraft there are particularly two modes that have the ability to accumulate energy and that are felt unpleasant to the crew. These occur at around 4 and 12 Hz, even with no external equipment mounted at the fuselage or wings, (but in these cases the vibrations are moderate).

Various external equipment like antennas and radomes are mounted on the aircraft which alter the airflow into patterns that can be difficult to foresee. The result is an increased level of energy injected into the natural vibrational modes. A spherical radome attached to a cylinder with the same radius as the cylinder is mounted under the fuselage slightly behind the wings, see figures 1.1 and 1.2. The radome (AS-105DF) creates vortices and a complex turbulent wake that alters the behavior of the airplane. The wake impacts the aft part of the fuselage, the empennage, stabilizers and rudders, and may trigger violent vibrations.

Various attempts have been made to identify the vibration problem on the P-3C. Vibration measurements were taken by Lundberg already in 2000 [1], then by Lundberg and Skaugen in 2002 [2], and in 2004 [3], [4].

It was suggested that the cause of the vibrations was of aerodynamic origin, or more correctly expressed, the excitation mechanisms are of aerodynamic nature. Computational Fluid Dynamics (CFD) simulations were carried out for an area of the P-3C around and aft the radome by Reif and Wasberg [5], [6] that largely supported this hypothesis.

Vibrations cause stresses in the aircraft structures and on the long run they increase the probability to form cracks and fatigue. In this project, it has been a goal to understand the impact of the radome on the airflow and the consequences of the altered airflow on the aircraft. Using general aerodynamic principles together with computational fluid dynamics (CFD) simulations, a fairing with certain limits in extension has been designed, see figure 1.2. The fairing consists of a wedge that partly fills the space behind the radome with reduction in turbulent wake intensity. It has a fillet that weakens the related horseshoe vortex and moves it slightly out from the airplane fuselage and it has a pair of vortex generators that counteract the unsteady vortices shed by the radome. The result is a wake with reduced oscillatory fluctuations, reduced width, and that is moved slightly away from the fuselage. The transverse forces and torques generated by the airflow of the radome and fairing are reduced compared to the case with radome only, resulting in a weakening of forces that trigger the oscillations.

1.1 The test program

The test program were divided into various flight modes. An attempt was made to fly with constant airspeed and altitude for a sufficiently long time to make conditions constant and stable for recording of vibration data. It should be noted that the listed airspeeds are only approximate. True airspeeds are measured during each data recording. Attempts were made to get as smooth flying conditions as possible during the tests with minimal atmospheric turbulence since the presence of moderate or stronger atmospheric turbulence would add unwanted noise to the data.

The data was recorded with varying airplane weights, at varying speeds, with and without auto pilot, flying at constant altitude, except for the “power setting” flight tests. Some special maneuvers were carried out during a minor number of measurements during various power settings, each with constant speed but changed altitude, and finally “double rudder”. A maneuver that creates a certain yaw angle during flight. The five independent flight parameters are summarized in table 1.1.

Airspeeds in kt	200	240	280	320	360
Weights in 10^3lbs	105	120	135		
Power settings HPs	500	1500	2500	3500	
Double rudder					
Auto pilot	on	off			

Table 1.1 Flight parameters.

Figure 1.1 The P-3C aircraft with the radome mounted below the fuselage.

Figure 1.2 The fairing (in pink) mounted on the radome and fuselage.

2 Measurements of vibrations

2.1 Equipment for vibration measurements

The vibration measurements were carried out using 15 accelerometers. They were attached in 9 different positions as shown in figure 2.1. One-axis accelerometers were used single or in pairs according to needs.

All accelerometers were delivered by KISTLER. They were mounted for recording in vertical (z-direction) and spanwise or transverse direction (y-direction) to the main structure of the airplane framework, see table B.1. In some locations, the accelerometers are glued in pairs on a metal block that is glued to the airplane frame. Figures 2.2 and 2.3 shows two examples of a two-block mounting in the empennage1 and aft boom, respectively.

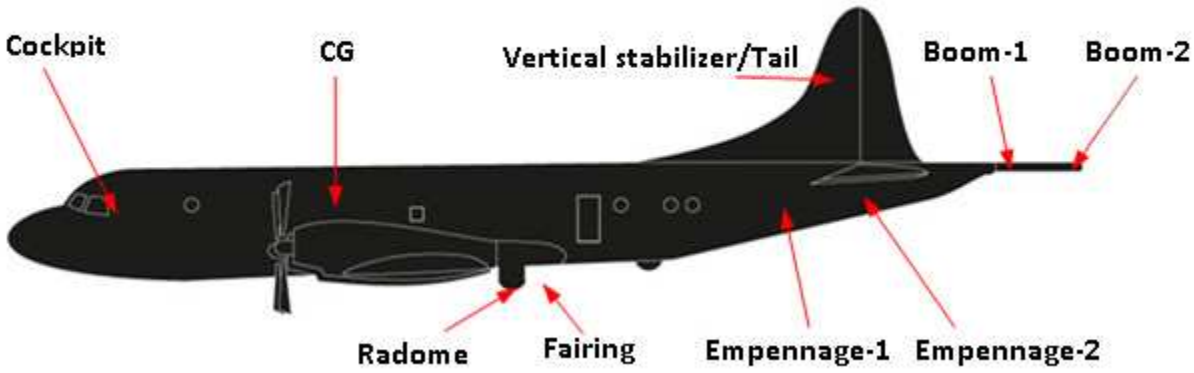

Figure 2.1 The P-3C aircraft with sensor positions.

2.2 The accelerometers

The K-beam accelerometer is able to measure frequencies between 0 to 250 Hz by using a sensing element which consists of a small inertial mass and a flexure element cantilever positioned between two plates. As the mass deflects under acceleration, the capacitance between these plates changes. AC excitation and synchronous amplitude demodulation circuitry contained in the accelerometer's signal conditioner provides an analog output signal proportional to the applied acceleration. All units are in $g = 9.81\ m/s^2$. A 12 V battery was used to drive the accelerometers in order to get as low noise as possible. Data and positions of the accelerometers are listed in Appendix B.

Figure 2.2 Accelerometer mounting at empennage1.

Figure 2.3 Accelerometer mounting at boom2.

Figure 2.4 Accelerometer mounting at empennage2.

2.3 Sensors mounting

The accelerometers were glued directly to the surface using a strong adhesive, giving a good connection to the material. Two accelerometers were glued to a cube which then was glued to the surface at the positions where both the Y and Z directions were measured. The accelerometers in empennage2 were glued on to a metal plate together with the Inertia Measurement Unit (IMU), see figure 2.4. This can have some influence on the data recorded in empennage2.

2.4 Logging equipment

Measuring acceleration and inertial data could not be done on a single unit so three different units were used in the measurements. The cDAQ-9172 is an USB 2.0-compliant eight-slot NI CompactDAQ chassis that can hold up to eight C Series I/O modules. Four NI 9234 C-series accelerometer acquisition modules were used to measure the accelerometers, and a NI 9239 C-series voltage acquisition module was used to measure a 5V synchronization signal. The cDAQ-9172 powered by the Yuasa battery and was connected with a USB cable to the HP laptop. The measurement equipment was positioned on a table in the “kitchen area”. In order to secure the equipment, a wooden plank was cut to fit the table and aluminum brackets were mounted to the plank to ensure that the equipment was held in place. The wooden plank was then fastened to the table with lashing straps as shown in figure 2.5 below.

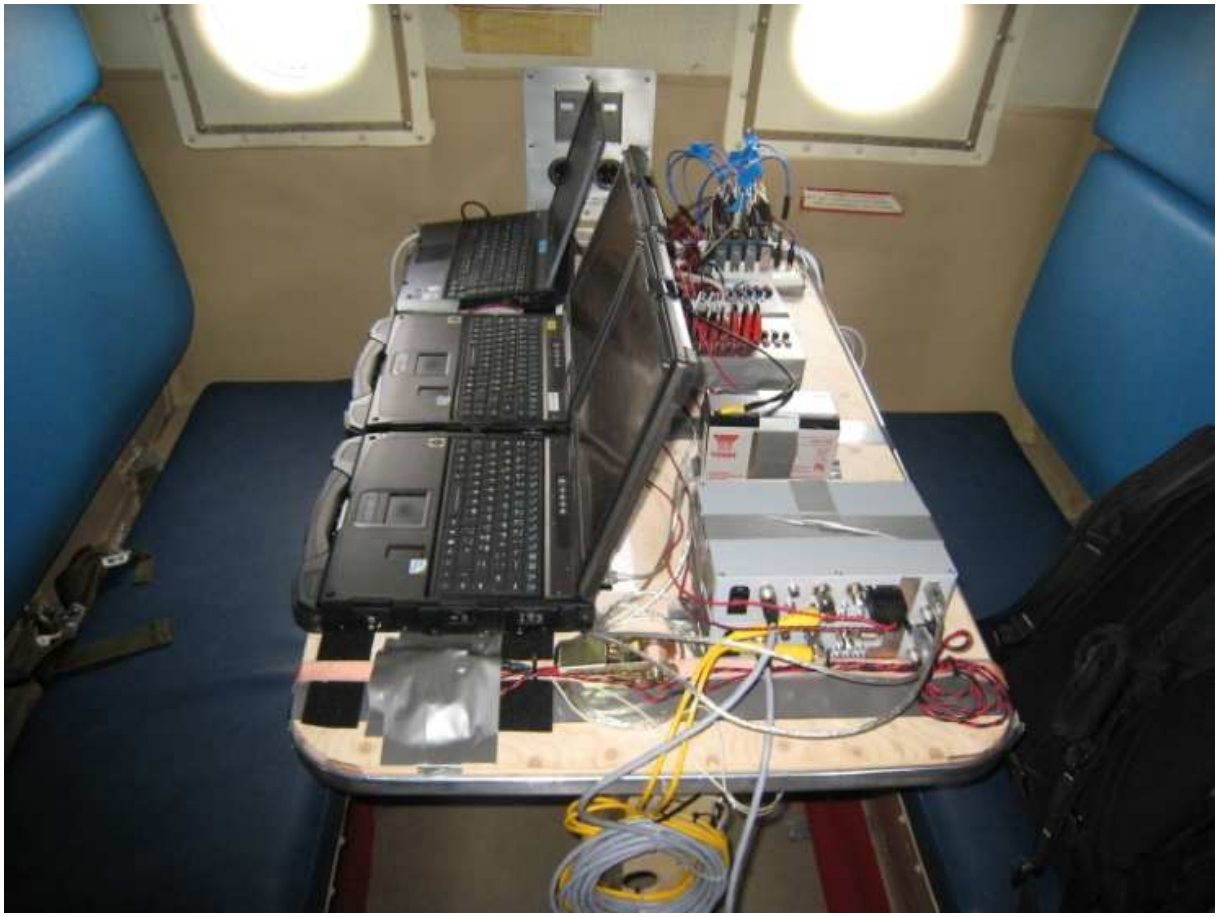

Figure 2.5 Logging station.

Two SiMU02 digital micro-electromechanical IMUs consisting of 3 accelerometers and 3 gyros were included in the instrument package. One IMU was attached in CG while the second was attached in empennage 2. Unfortunately, some electrical noise from the airplane power supply cause distortion of the data, in particular for the 280 and 320 kt and 130.000lbs weight case. The noise, possibly electrical transients, damaged the electronic record system for the IMUs so no data was recorded from the IMUs. Fortunately, with the exception of a few recordings at 130.000lbs weight, all accelerometer data are of high quality.

3 Experimental Results

3.1 Analysis of the accelerometer data

The accelerometers used for the P-3C tests were able to gather information in the low frequency range (0 - 250 Hz). Unprocessed data are shown in figure 3.1. The relevant frequency range for metal fatigue studies in airplanes is (0 - 15 Hz). According to power spectra, see for example figure 3.8, there is energy all over the spectrum, but since this study is related to metal fatigue, we concentrate our effort in the (0 - 15 Hz) frequency range. There are two peaks at 4 and 12 Hz that are present in nearly all of the power spectra, that are of importance. That is the reason that most of the derived quantities will be calculated in the range (0 - 15 Hz). The accelerometers were sampled in the frequency range (0 - 5000 Hz). We applied a low pass filter to obtain physical relevant data. The low pass filtering can be done by truncating data in frequency space for Fourier transformed data or in physical space by applying a Butterworth filter. An example of raw acceleration data and low pass filtered data at 50 Hz, for comparison, is given in figure 3.2. *Notice that in all analysis involving calculation of RMS data and calculation of sensor displacements, low pass filtered acceleration data at 15 Hz are used in the calculations.*

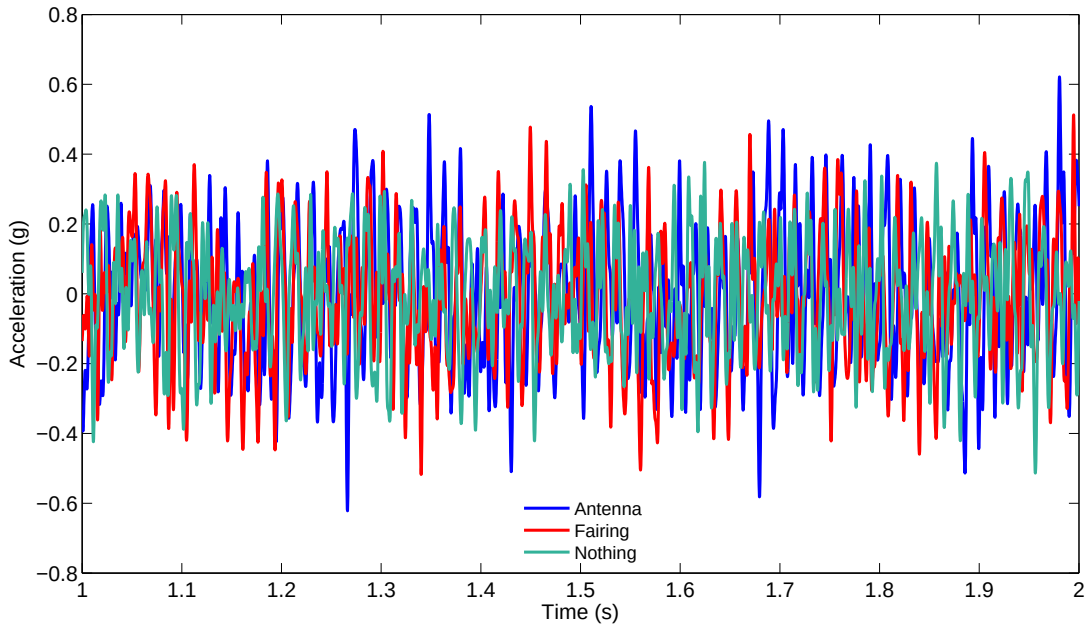

Figure 3.1 Accelerations in the transverse direction at the vertical stabilizer when the weight of the aircraft is 135 000 lbs and speed is 240 kt.

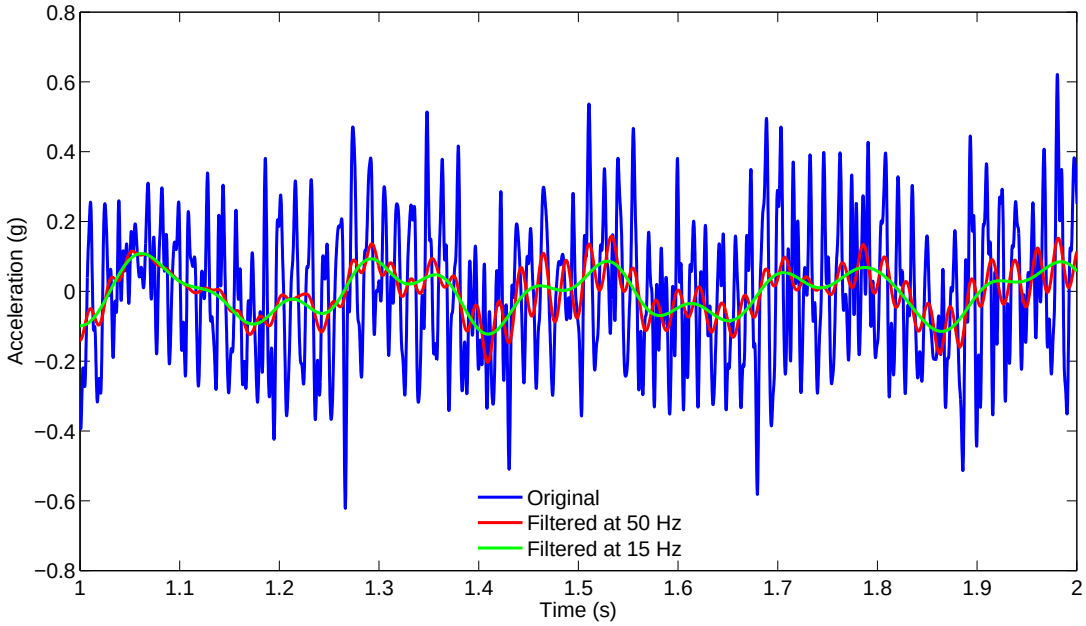

Figure 3.2 Acceleration of the vertical stabilizer in the transverse direction for weight of 135 000 lbs and speed 240 kt.

The measurement campaign was carried out for three main configurations. These were

1. Flight with AS-105 DF antenna/radome attached with the passive flow control device (which is named *fairing*)
2. Flight with AS-105 DF antenna/radome only
3. Flight with no radome and no fairing

A snapshot of the time history of the low-pass filtered acceleration signal from each of the 15 sensors which were placed over the aircraft when the radome was present are grouped in figures 3.3 and 3.4 for transverse and vertical directions, respectively. The figures indicate large vibration readings (the dashed lines) on the boom of the aircraft. This is expected because of the slenderness of the structure which is at the very back of the aircraft, and because vibrations are expected to increase with distance from CG. The largest vibrations, sorted after the slender boom were observed by the sensor placed in the vertical stabilizer (also denoted as tail in this report).

For the further analysis, the following data were derived from the low pass filtered accelerometer data (see A.3 for details):

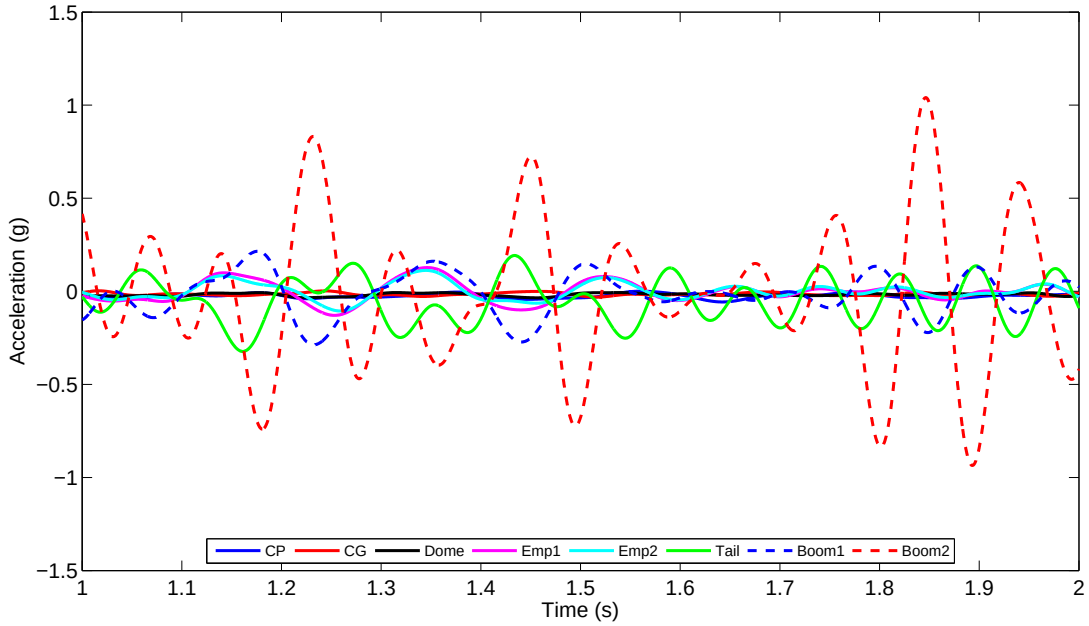

Figure 3.3 Low pass filtered accelerations in the transverse direction for weight of 120 000 lbs and speed 320 kt (with radome).

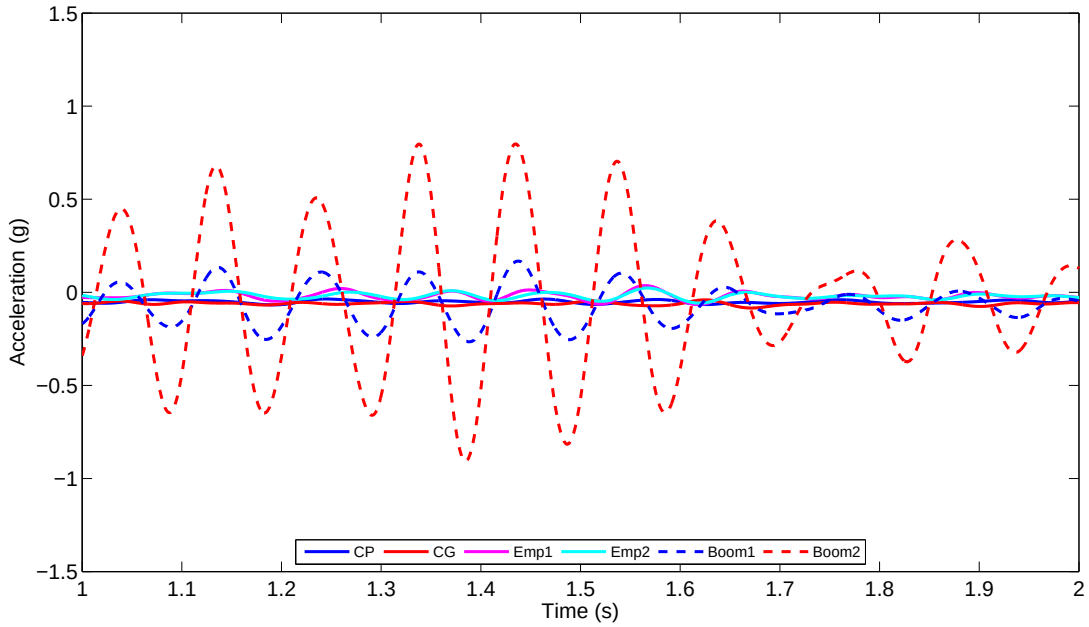

Figure 3.4 Low pass filtered accelerations in the vertical direction when the weight of the aircraft is 120 000 lbs and speed is 320 kt (with radome).

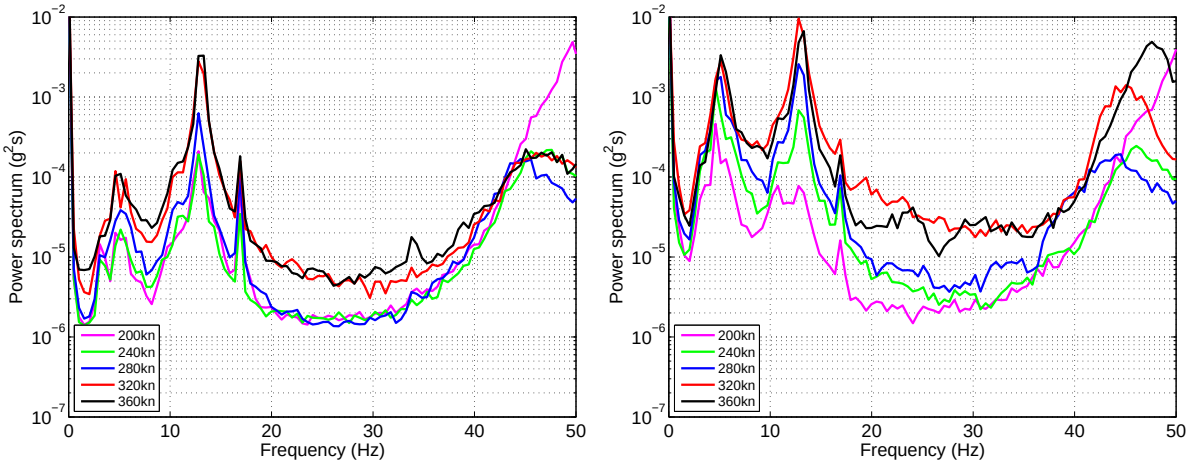

(a) Without radome (b) With radome

Figure 3.5 Power of transverse accelerations at the vertical stabilizer when the weight of the plane is 120 000 lbs.

- Power spectra are derived in the range (0 - 50 Hz)
- Root-mean square (RMS) values are calculated from acceleration data in the frequency range (0 - 15 Hz)
- Fluctuating transverse and vertical displacements are calculated in the frequency range (0 - 15 Hz)

The fluctuating transverse and vertical displacements express the structural “bending” of the airplane and can be used to identify whether metal fatigue may be a problem or not.

3.1.1 Power spectra

Effect of attaching the radome is best seen by comparing the power spectra of the vibrations registered by the sensors at two different situations; namely readings during the test without and with radome. As the speed of the aircraft increases, the vibrations observed at the tail increase regardless of attached or removed radome. This behavior can be seen in the power spectra curves presented for different velocities in figure 3.5. The figure shows that the vibrations experienced by the vertical stabilizer are large at around 12 Hz even when the radome is not attached to the aircraft. Amplification due to the attached radome is apparent at the vertical stabilizer such that power spectra obtained at different velocities are almost elevated by one decade regardless of the speed of the aircraft. This is even more pronounced at a particular lower frequency at around 4 Hz.

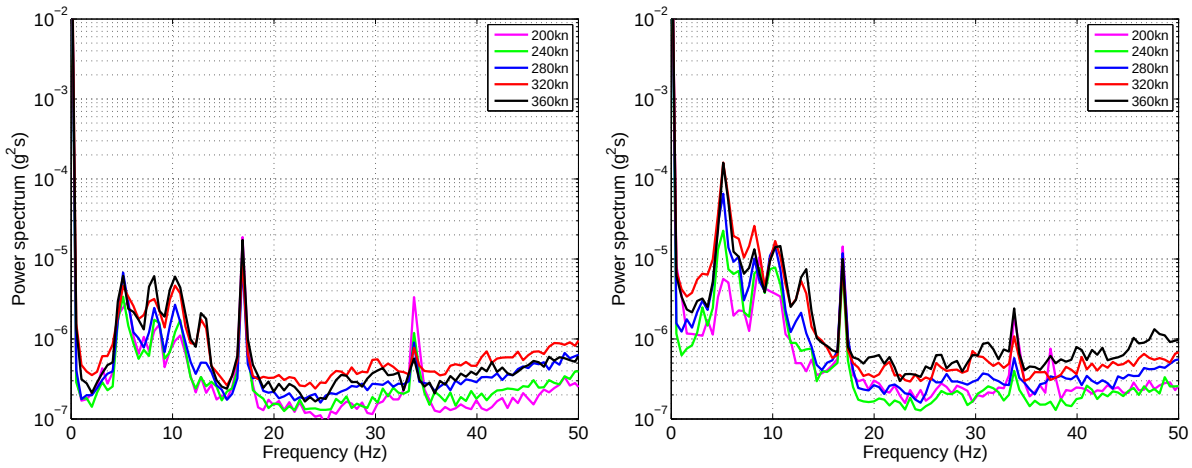

(a) Without radome

(b) With radome

Figure 3.6 Power of transverse accelerations in the cockpit when the weight of the plane is 120 000 lbs.

A similar picture is presented in figure 3.6 in order to show the sensor readings in the transverse direction in the cockpit area. The power spectrum at all frequencies are modified when the radome is attached to the aircraft. The change caused by the radome seems to be localized in particular from (0 - 15 Hz). The magnitude of the vibrations in the cockpit area is certainly less than that on the vertical stabilizer. *Note that the peaks in the spectra at 17 and 34 Hz are caused by the propeller*. Notice also the relatively high power in the propeller noise at these frequencies in figure 3.6. Evidently the propeller noise is relatively reduced compared to the full noise picture in the vertical stabilizer, see figure 3.5.

Figure 3.7 presents the power spectra of the transverse acceleration signal from the vertical stabilizer for three different aircraft weights while the speed was kept constant at 240 kt. This figure, in light of figure 3.5(b), indicates that the vibrations caused by the radome depend more on the speed of the aircraft than on the varying weight.

Figure 3.8 presents the power spectra of the transverse acceleration signal in the vertical stabilizer. The figure is organized for all five different velocities tested during the experiment campaign. Each subplot show the power spectra of the signal when only the radome was present, when the radome was present with the attached fairing, and when neither was present. The figure shows that the vibration occuring when only the radome is present increases as the speed increases from 200 kt to 360 kt. Unfortunately, the 320 kt data (for the flight with radome only) were corrupted and could not be used in this analysis. All figures displaying power spectra are here presented in semi-logarithmic fashion such that small differences in the vertical direction indeed indicates large differences. In all velocities (from 200 kt to 360 kt), there appear to be an amplification of the low

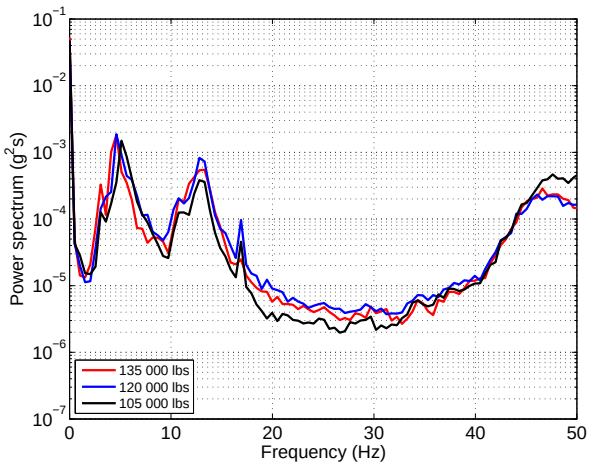

Figure 3.7 Measured transverse accelerations at the vertical stabilizer for three different aircraft weights when the speed of the plane is 240 kt.

frequency vibration energy of nearly two orders of magnitude between flights with and without radome. This is in particular true where we observe peaks in the spectrum, e.g. at 4 and 12 Hz.

The fairing in the cases shown in this figure works almost perfect at frequencies above 12 Hz as it kills almost all significant vibrations from (12 - 50 Hz) caused by the radome. The performance of the fairing is also relatively good in the low frequency part of the spectrum. Here, the RMS values of acceleration are reduced by 50% compared to the values with radome only and the values for clean airplane. The fairing reduces the vibrations at all airspeeds. This is most pronounced in the vertical stabilizer and the two positions in the boom, but also in empennage1 and empennage2. Inside the pressurized area of the aircraft, the reductions are not that pronounced. The pressurized cabin is stiffer than the rest of the aircraft, which is probably the reason for less vibrations there, see figures 3.9.

Further quantification of the performance of the fairing can be seen in figures 3.9 and 3.10, where the power spectra of the sensor placed on the aircraft are grouped according to the direction they measure and conditions the tests were performed; namely radome only and radome with fairing. The results show that the fairing reduces the vibrational energy at every position on the aircraft.

The strongest vibrations in the boom are slightly above 10 Hz, see figure 3.9. The vertical stabilizer has about the same power in the 4 and 12 Hz modes, while the rest of the sensors show maximum energy at 4 Hz where the 12 Hz mode is less pronounced. The boom seems to have its own vibration pattern due to its local stiffness and mass. Perhaps the boom vibrations also propagate into the vertical stabilizer and causes its 12 Hz mode. It is possible to reduce the vibrations in the boom both aerodynamically by reducing the intensity of the radome wake, and mechanically by altering its stiffness and/or mass.

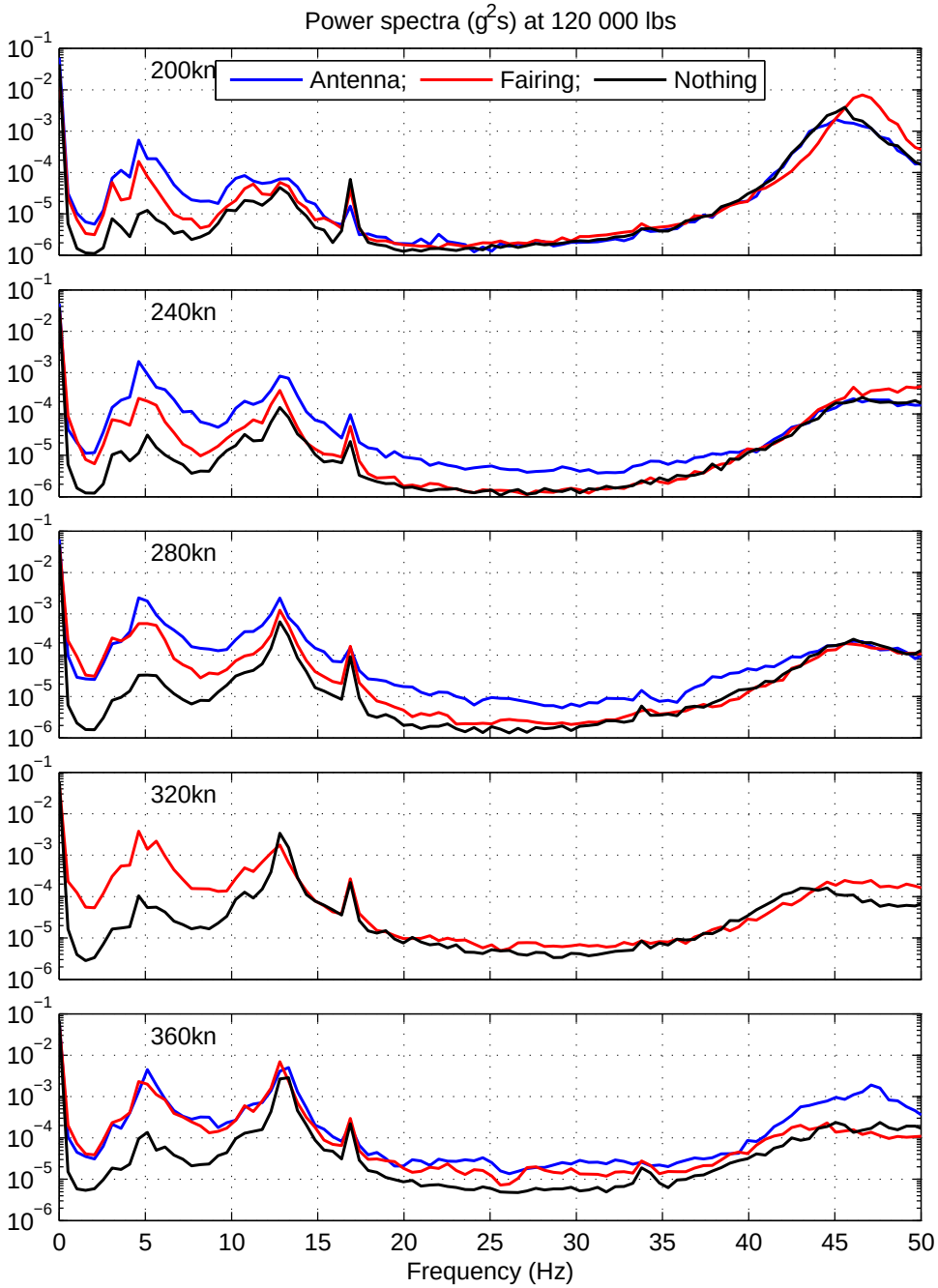

Figure 3.8 Power spectra of the accelerations, in the transverse direction, at the vertical stabilizer when the weight of the airplane is 120 000 lbs.

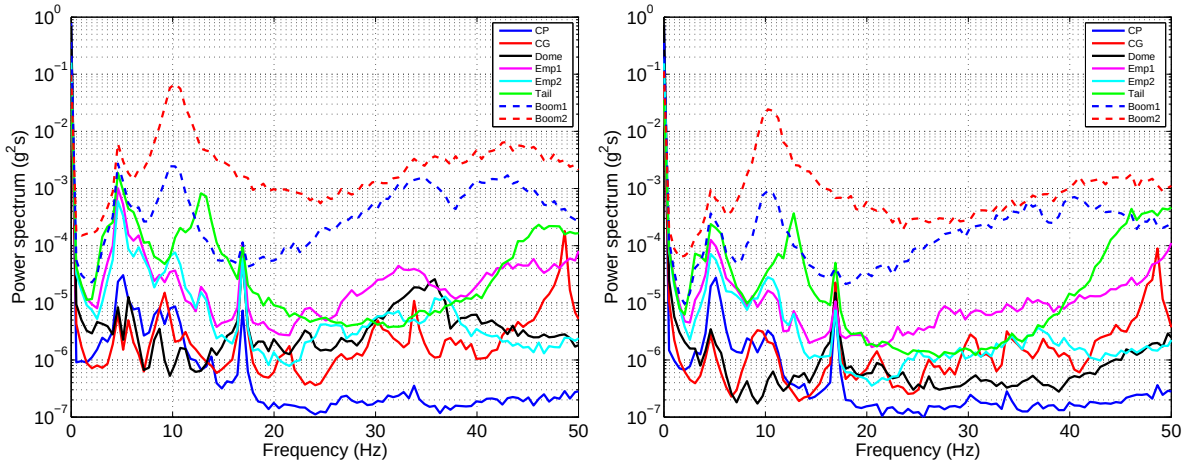

(a) Radome only (b) Radome with fairing

Figure 3.9 Power spectra of the transverse direction vibrations on every sensor located on the plane (Weight: 120 000 lbs. Speed: 240 kt).

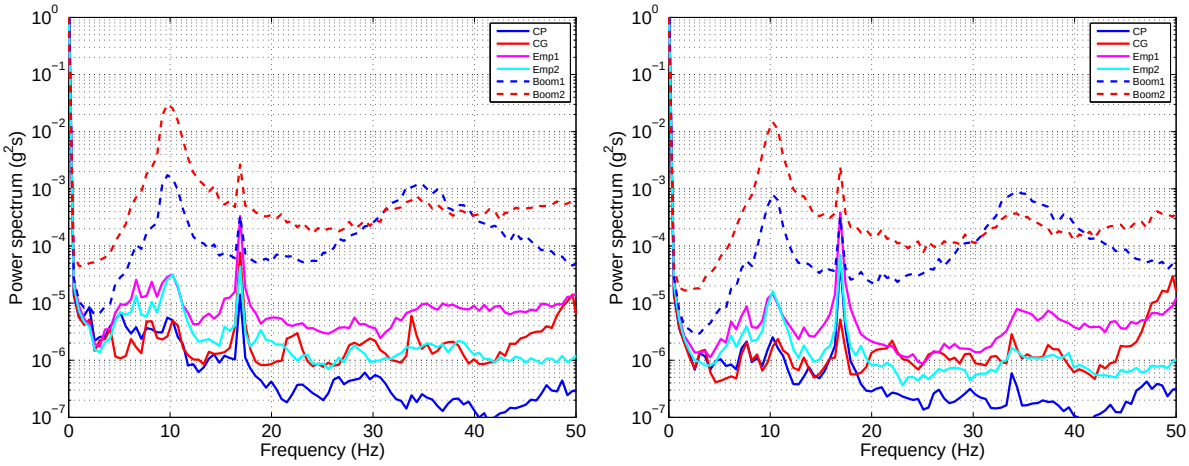

(a) Radome only (b) Radome with fairing

Figure 3.10 Power spectra of the vertical direction vibrations on every sensor located on the plane (Weight: 120 000 lbs. Speed: 240 kt).

3.1.2 RMS values

The radome, as seen from the presented results, amplifies the vibrations experienced by the aircraft. On the other hand, the fairing functions and reduces the low frequency vibrations. Even though it is difficult to see the performance of the fairing from the trace of the acceleration signal clearly, it clearly shows up when calculating the RMS of the acceleration data.
The most significant conclusion that can be drawn from the data analysis of the accelerometer data that is relevant for metal fatigue of the airplane structure follows below. By calculating the RMS of the fluctuations of all data in the frequency range (0 - 15 Hz), we get an overall picture of the vibrations recorded over three days of measurements:

- Radome: The vibrations are the strongest in all cases. Maximum RMS level is 0.6g
- Radome and fairing: The RMS accelerations are maximum 0.45g. Accelerations are all over reduced by 50% compared to noise with radome alone
- Clean airplane: The vibrations are still there. Maximum RMS level is 0.3g

The RMS values from all sensors, both transverse and vertical directions, are shown in figures 3.11, 3.12 and 3.13. Note that for weights 105.000 lbs through 135.000 lbs, presented in figures 3.12 through 3.19, increasing flight test number means either equal or increasing air-speed.

It is interesting to note that the RMS of acceleration in the transverse (or yaw) and vertical directions for some of the accelerometer locations decreases with increasing airspeed when the radome is on. This is experienced by the pilot and crew. For radome with fairing this effect is not so pronounced, and for clean airplane the vibrations increase with airspeed in all sensor locations. This can be seen in figures 3.14 - 3.19.

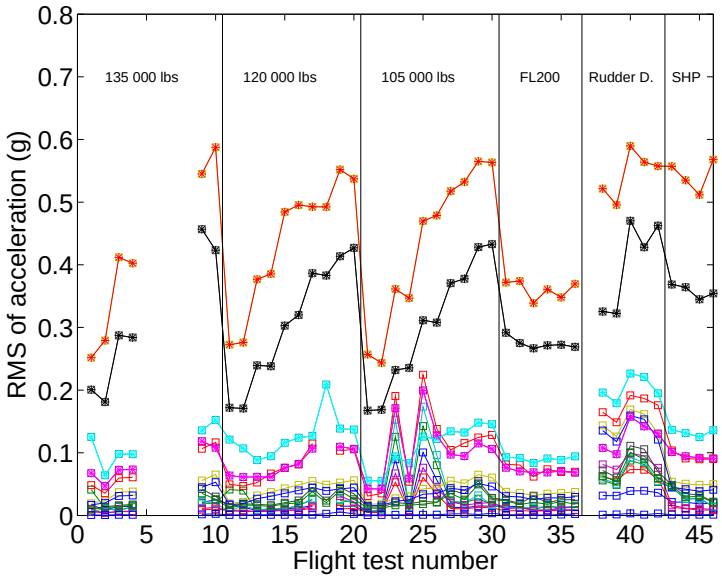

Figure 3.11 *RMS data of acceleration for airplane with radome only. Some data are lost due to electrical noise. The red curve (max) shows RMS values of transverse acceleration while the black curve shows RMS values of vertical acceleration, both in the aft part of the boom. The other curves show the transverse and vertical RMS values of acceleration for the successive sensor groups.*

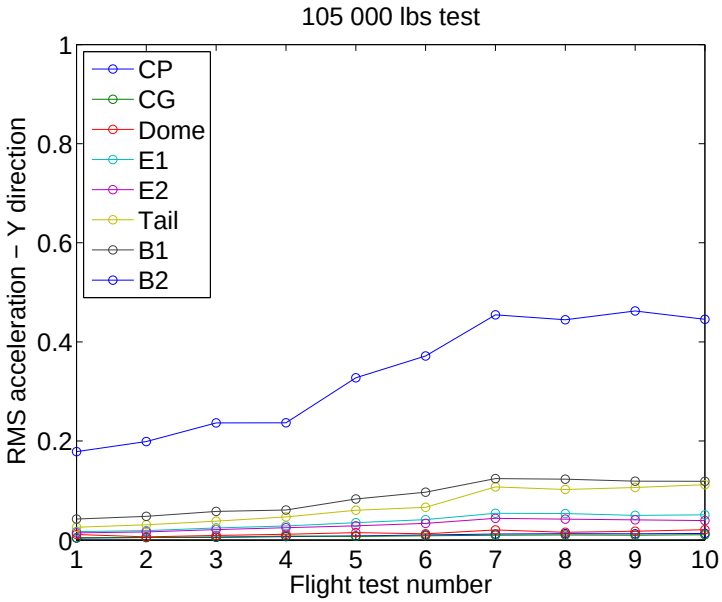

Figure 3.15 *RMS data of transverse acceleration for airplane with radome and fairing.*

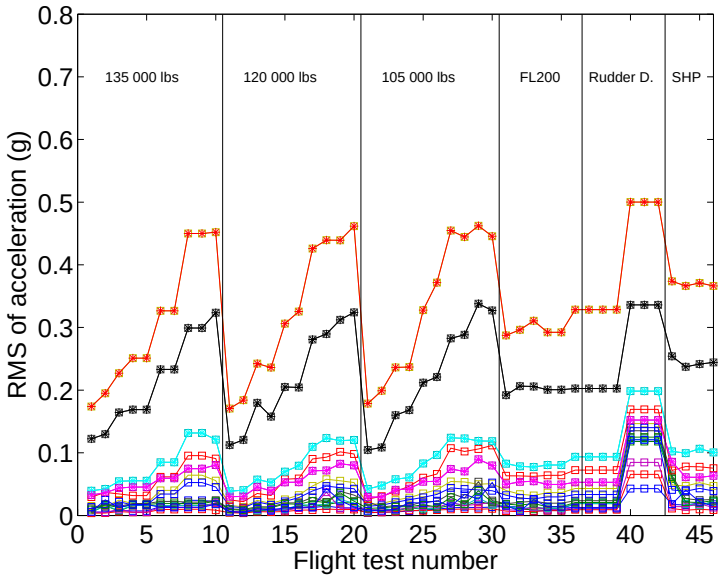

Figure 3.12 RMS data of acceleration for airplane with radome and fairing. The curves are explained in figure 3.11.

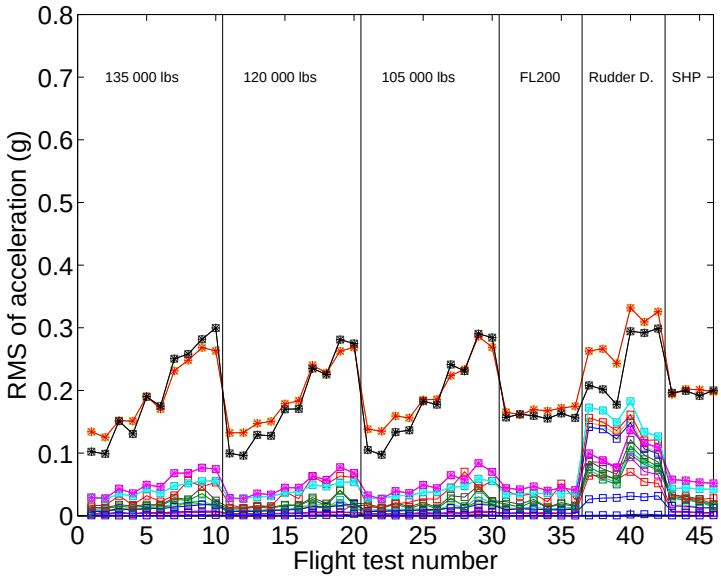

Figure 3.13 RMS data of acceleration for airplane without radome (clean airplane). The curves are explained in figure 3.11.

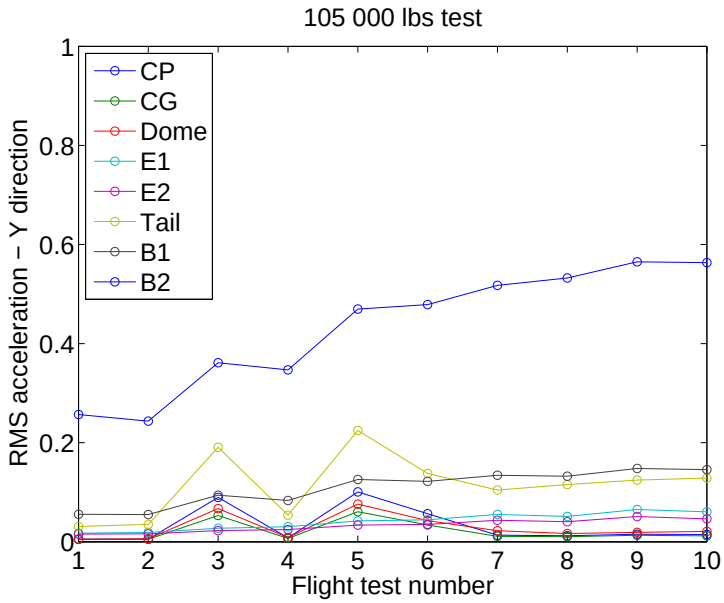

Figure 3.14 RMS data of transverse acceleration for airplane with radome only.

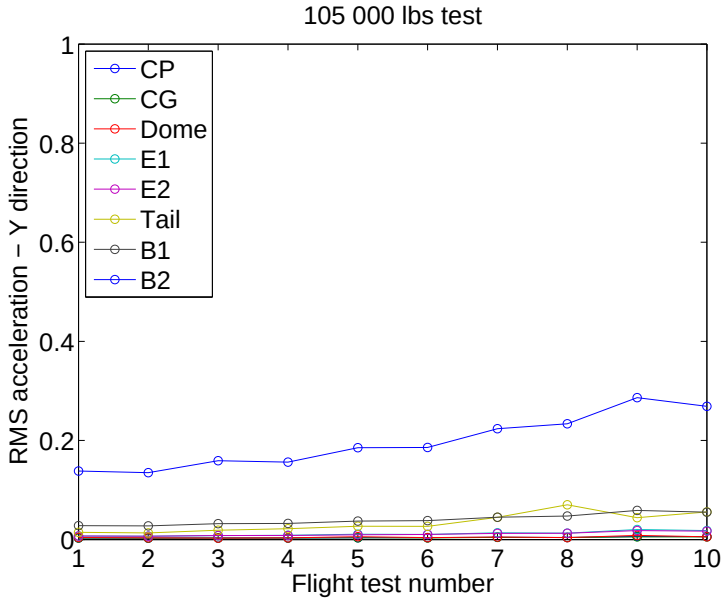

Figure 3.16 RMS data of transverse acceleration for airplane without radome and fairing (clean airplane).

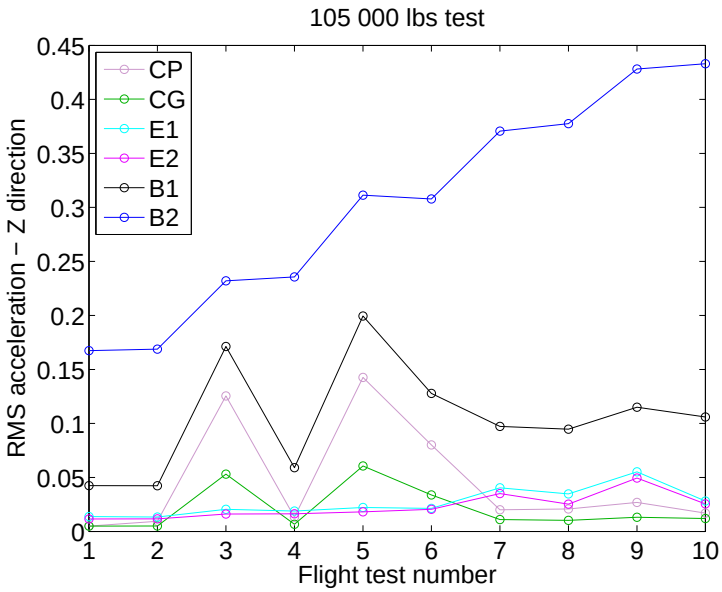

Figure 3.17 RMS data of vertical acceleration for airplane with radome only.

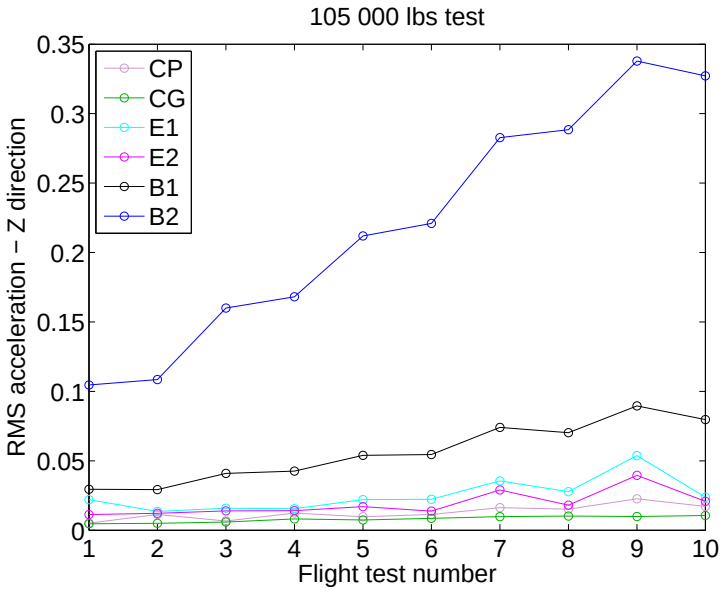

Figure 3.18 RMS data of vertical acceleration for airplane with radome and fairing.

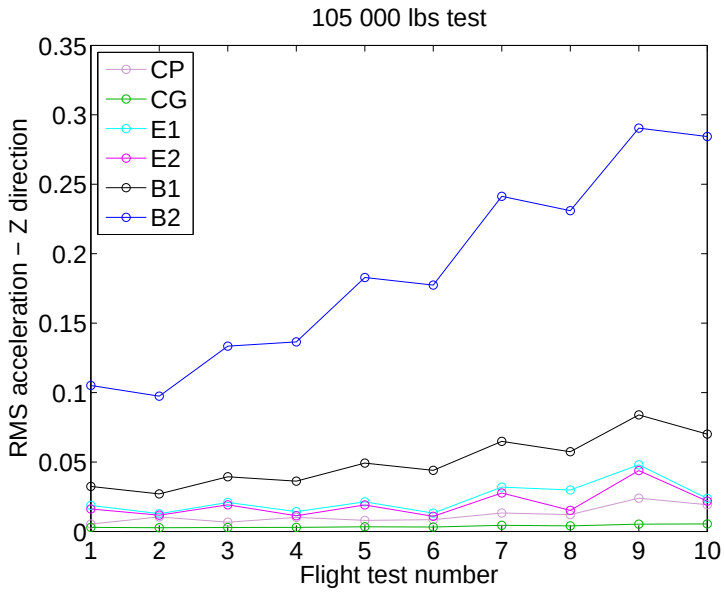

Figure 3.19 RMS data of vertical acceleration for airplane without radome and fairing (clean airplane).

3.1.3 Displacement

The acceleration data also give access to computation of local displacements in time by integration of the acceleration data over time as described in A.3. The velocity of a sensor is computed by integrating the filtered acceleration and integration of velocity gives the displacement. Figure 3.20 shows the displacement of the sensors in the transverse direction as a function of time. As expected, the motion in the rear part of the airplane is opposite in direction compared to the motion of the cockpit most of the time, but not always. Also, it is noticeable that the displacement in the rear part of the boom is much larger compared to the displacement of the cockpit area.

Displacement data can be visualized as time-series. At each instant, the displacement of each sensor is plotted. The sensor positions (x_i, y_i) are plotted in Cartesian coordinates (x, y) where the x_i coordinate is the distance from the nose of the airplane to sensor i, while y_i is the transverse displacement of sensor i. In the same way the vertical displacements are visualized. Here, coordinates (x, z) are used.

These plots show the "bending" of the aircraft as a function of time. In figure 3.21, the accelerometer positions for transverse direction for three different instants are shown. Notice that the curves deviate from straight lines, which mean that the airplane is flexing and bending. The displacement is strongest in the boom. In figure 3.22, the envelope is shown, revealing the extrema of the transverse displacement of all sensors, by plotting displacement curves continuously on top of each other over

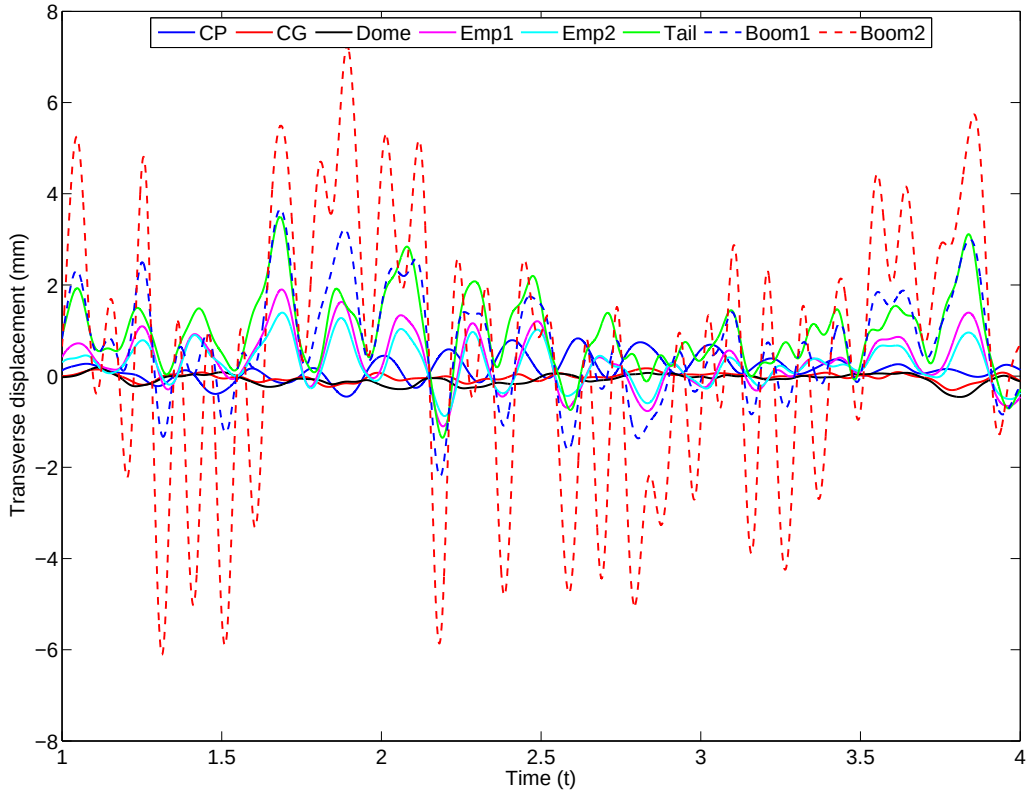

Figure 3.20 Displacement in the transverse direction when weight is 135000 lbs and airspeed is 240 kt.

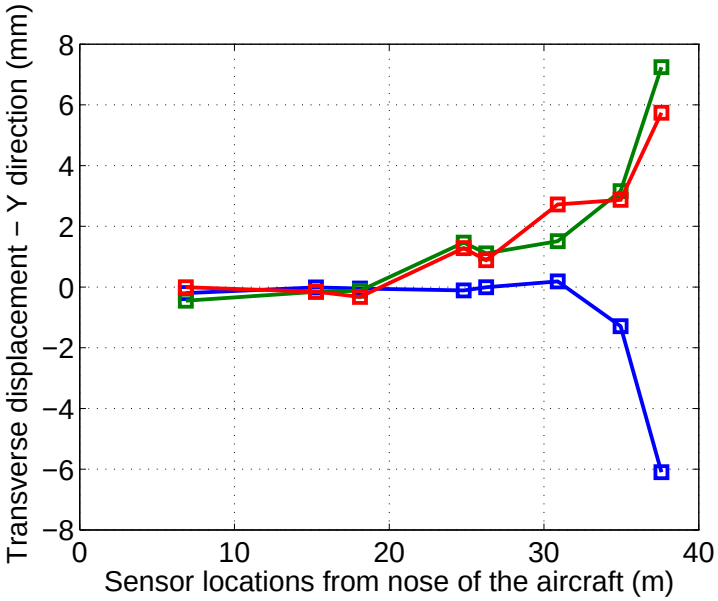

Figure 3.21 *Displacement in the transverse direction for when weight is 135000 lbs and airspeed is 240 kt. Displacement is shown for each sensor position, revealing the "bending" of the airplane at three different times (red, green, blue).*

a selected period of time. There are instants where higher wave modes are present, where the curve connecting the various accelerometers are not strictly monotonically decreasing or increasing. There is an indication of this in all three curves shown in figure 3.21. Sometimes, empennage1 has a bigger displacement than empennage2 and the tail. It is beyond the scope of this report to study motion in such detail but the quality of the current data is probably good enough for such information to be derived.

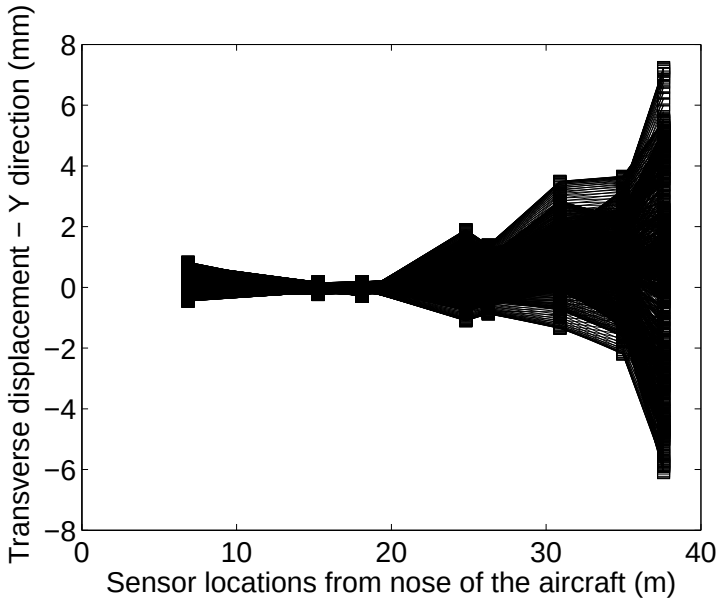

Figure 3.22 Displacement in the transverse direction for when weight is 135000 lbs and airspeed is 240 kt. The displacement is shown for many instants revealing the envelope of the sensor displacement.

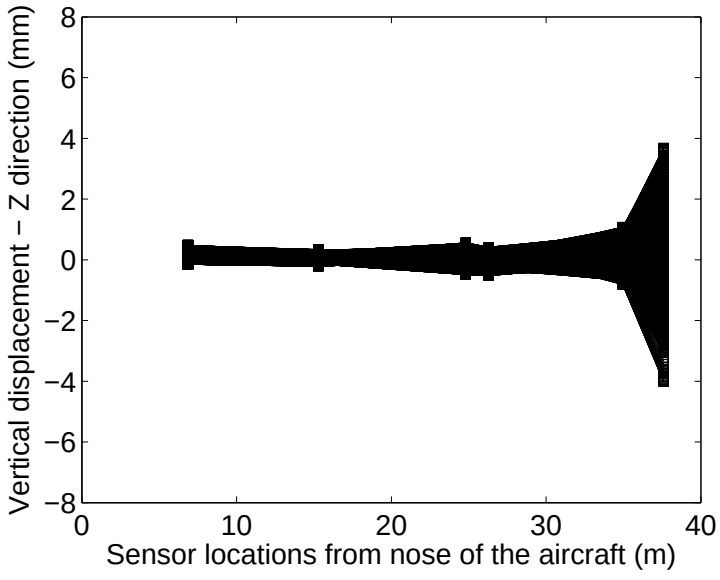

Figure 3.23 Displacement in the vertical direction for when weight is 135000 lbs and airspeed is 240 kt. The displacement is shown for many instants revealing the envelope of the sensor displacement.

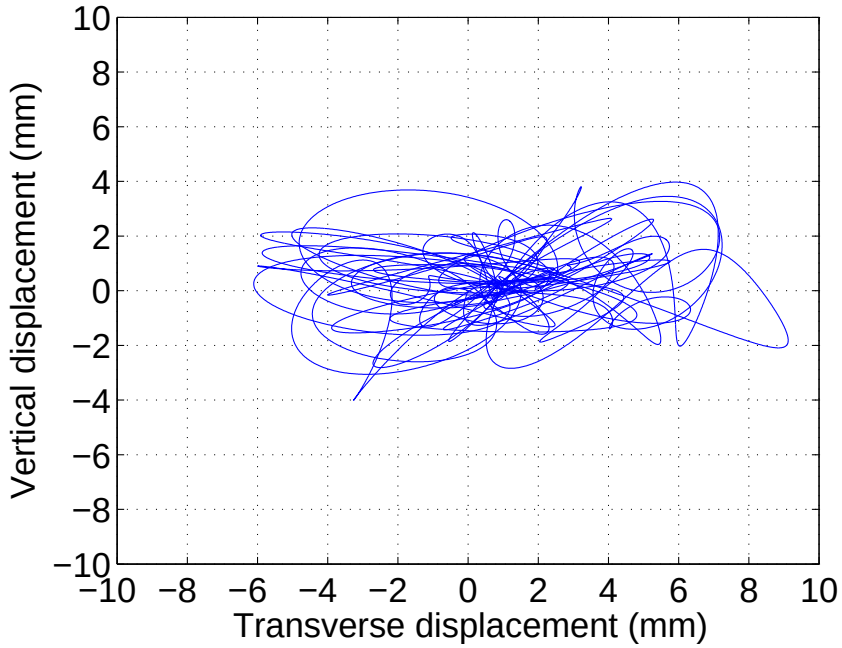

Figure 3.24 The path of the aft boom sensor pairs (strange attractor) over 5 seconds time span, the data are the same as used for figure 3.21 and 3.23.

Since we know the displacement in the transverse and vertical directions it is possible to visualize the motion of each sensor pair in a plane as a path line. In figure 3.24, we show the path of the aft boom sensor pair sampled over 5 seconds. The path line stays around a center as a “strange attractor” and has an elliptic shaped outer perimeter, but except from that the motion is stochastic.

4 Numerical simulations

The primary objective of the simulations is to model the flow field in the vicinity of the radome in sufficient detail to reproduce the unsteady shedding responsible for the observed low frequency vibrations.

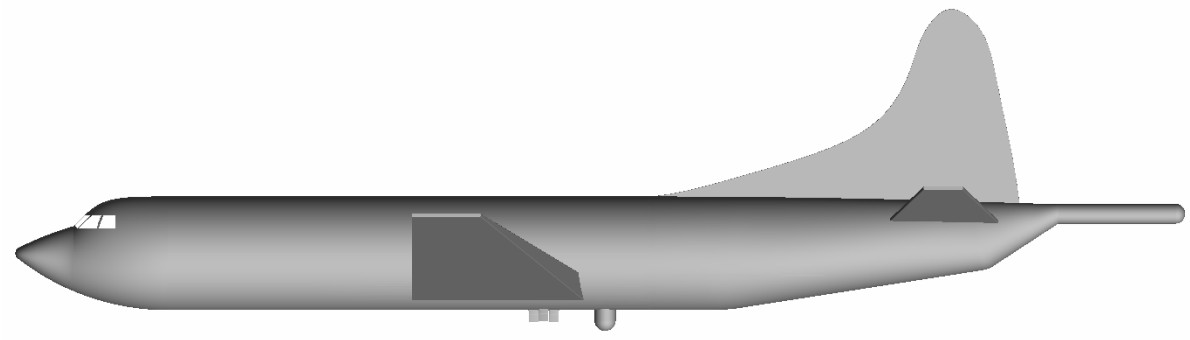

Figure 4.1 A simplifed model of the P3-C.

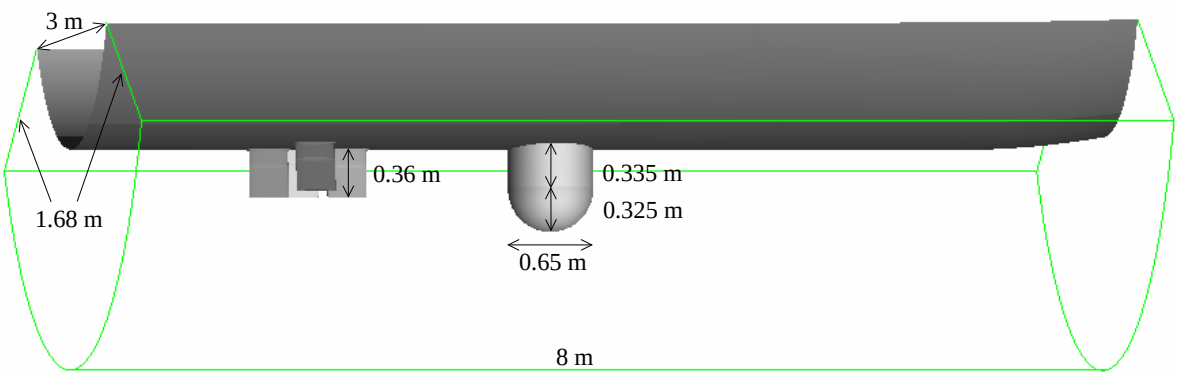

Figure 4.2 The part of the aircraft body used in the numerical simulations.

A simplified model of the P3-C aircraft is shown in figure 4.1. A numerical simulation of the the flow around the full aircraft is not feasible with the desired level of detail and the available computational resources. The problem is therefore restricted to simulating the flow around the the aircraft body near the radome. Apart from the four ACSL and Dual Band antennas situated 1-2 m in front of the radome, no geometrical details are included in the model. The full computational domain, extending 1.7 m out from the fuselage, is shown in figure 4.2.

This simplified configuration does not take into account two major effects on the aircraft. Firstly, the downward effect from the wings, and secondly the propeller slip-stream. These effects greatly modifies the flow field aft the radome. However, the fundamental mechanisms responsible for the

unsteady forcing are associated with the local wake dynamics downstream the radome rather than with the external flow field. The present configuration is thus sufficient to investigate the shedding and its associated *forcing* on the fuselage. In order to predict the *response* on the aircraft, the entire aircraft needs to be considered, including the engines.

The simulations are performed using the flow solver program Fluent from ANSYS Inc., solving the equations for incompressible, viscous fluid flow. The small-scale turbulent features are modelled using the Spalart-Allmaras RANS (Reynolds-Averaged Navier-Stokes) model [7].

4.1 Geometries

The configuration shown in figure 4.2 is that of the original radome without modification. A number of modifications, described in Appendix Appendix C, have been used in simulations as a part of the optimization process. The modification used in the simulations presented here is the latest suggestion, and is the design that was used for the flight tests described in this report.

4.2 Simulation runs and parameters

Speed (knots)	Radome only	Mod. 1	Mod. 2	Mod. 3	Mod. 3 15° sideslip
160				1.43	
280	1.39			1.21	
400	1.38	0.91	1.24	1.99	1.05

Table 4.1 Simulation end times (in seconds) for the different combinations of geometry and speed.

An overview of the performed simulations is presented in table 4.1. The computational domain is the same in all cases, except for the geometry around the radome. In the “Radome only” case, the original radome without modifications is used. Mod. 1, 2 and 3 refer to figures Appendix C.1(a)–Appendix C.1(c), respectively. The fifth configuration was “Mod. 3” with 15° sideslip, to check the sensitivity to yaw angles.

The simulations of different geometries were performed for flight speeds of 400 knots. As the flight plan for the experiments was developed, additional simulations were performed at lower speeds to match the experimental conditions and to check the sensitivity to flight speed.

4.3 Simulation results

The simulated vortices generated in the wake of the radome with and without modification are shown in figure 4.3. The plotted quantity is vorticity magnitude. Notice how the vortices in figure 4.3(b) have been lifted away from the fuselage by the aerodynamic modification. This effect

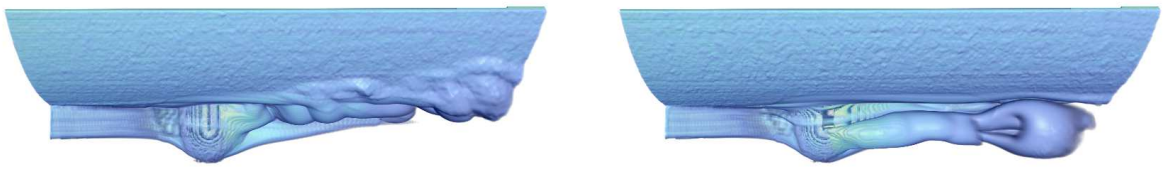

(a) Radome only

(b) Radome with modification 3

Figure 4.3 Vortices generated in the wake of the radome and the radome with modification.

constitutes the primary desired effect of the modification, since the expected consequence is less interaction with the tail section.

Figure 4.4 shows the same data as figure 4.3, but from a viewpoint below and downstream the radome. Notice how the modification design and in particular the *vortex generation plate* stabilizes the vortices in the wake of the radome (figure 4.4(b)) compared with the original design (figure 4.4(a)).

Figure 4.5 uses the same times and viewpoint as figure 4.4, but now the friction lines (i.e. field lines of the wall shear stress) are displayed. This illustrates the direction of the flow close to the surfaces. Again, we see that the effect of the modification is to narrow the area influenced by the vortices and reduce the sideways oscillations. The accumulation of field lines for the original configuration also indicate that the influence of the vortices is stronger at the fuselage than when the modification is used. Figure 4.6 shows the simulated vortices in the wake of the original configuration together with a model of the P3-C aircraft.

4.4 Power spectra of pressure forces

During the simulations, the pressure forces were integrated over different surface parts and saved at each time-step. The time-step for the simulations was set to 10^{-4} s. This means that the highest frequency that theoretically can be resolved is 5000 Hz. The lowest frequency is given by the simulation time. As seen in table 4.1, typical simulation times are 1-2 seconds, including a start-up period. For a sampling period of 1 second, 1 Hz is the lowest possible frequency that can be captured, but the amplitude at the lowest frequencies are less reliable than at the higher frequencies, as only one or a few periods have been observed. As we are primarily interested in the low frequencies in this study, the spectra are presented for frequencies from 2 to 50 Hz.

The pressure forces on different surface parts are shown in figure 4.7, in terms of power spectra. ”Total” refers to the integrated pressure forces over all the solid surfaces in the model, whereas

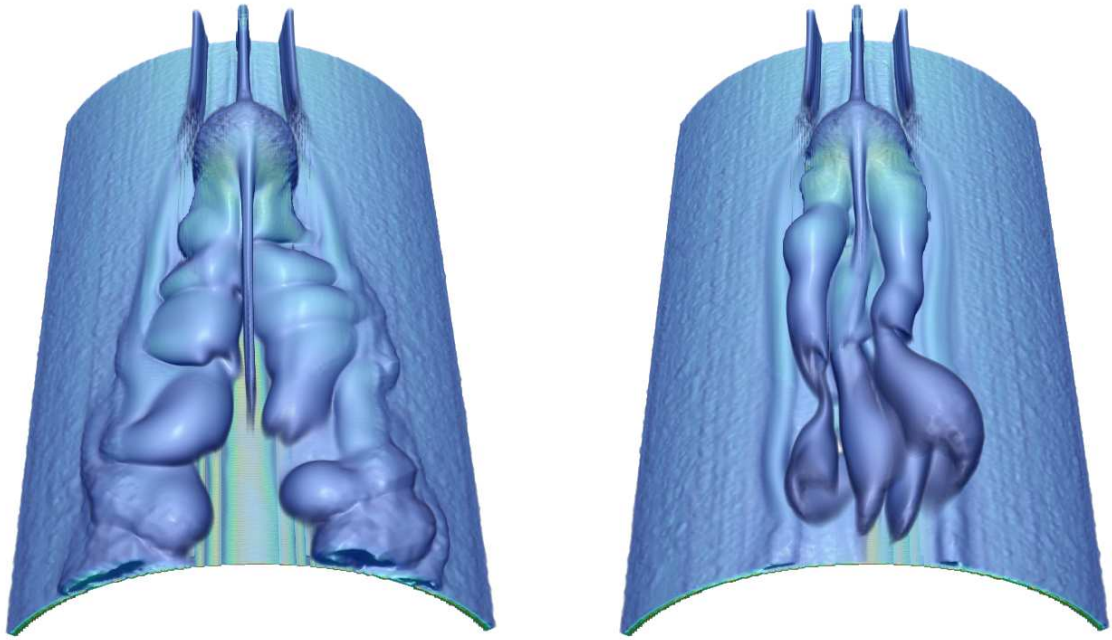

(a) Radome only (b) Radome with modification 3

Figure 4.4 Vortices generated in the wake of the radome and the radome with modification.

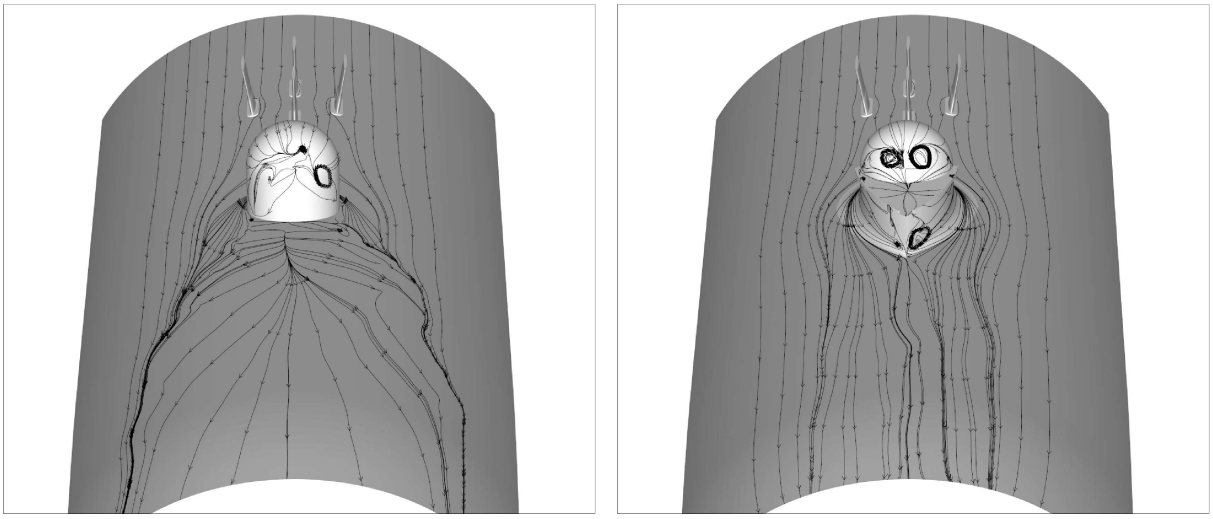

(a) Radome only (b) Radome with modification 3

Figure 4.5 Friction lines for "Radome only" and radome with modification.

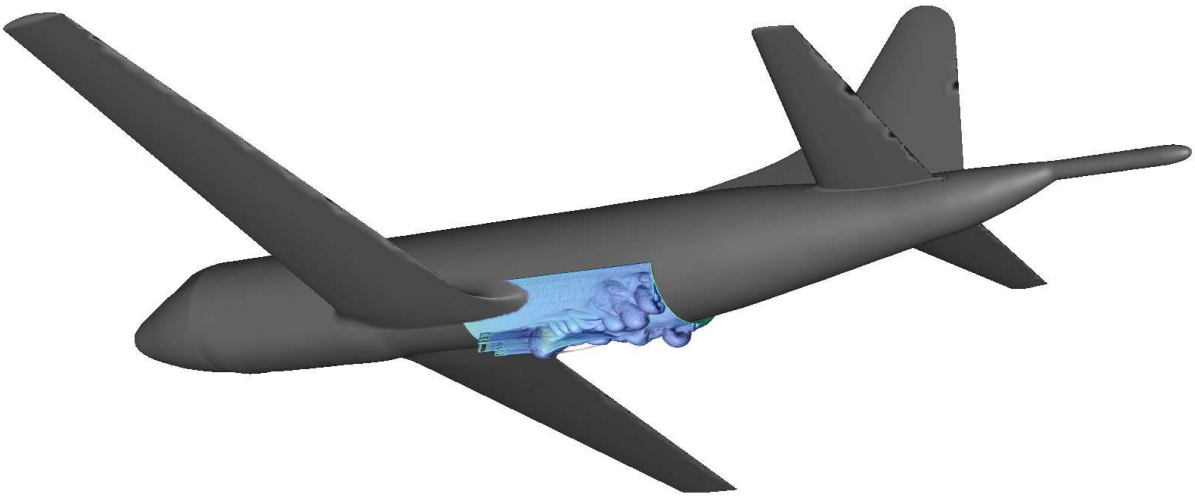

Figure 4.6 Visualization of vortices generated in the wake of the radome mounted on the P3-C aircraft. The simulated vortices are restricted to the simplified configuration used for the simulations (see figure 4.2) and does for instance not take into account effects from the wings.

"Fuselage", "Radome", "Wedge" and "Antennas" refer to integrated forces over those particular structures. "Wedge" is the surface of the modification, whereas "Radome" is the visible part of the original radome. "Antennas" are the ACSL and Dual Band antennas upstream the radome.

Figure 4.7(a) shows the power spectra of the transverse pressure forces. With the exception of the antennas, which are not directly influenced by the vortices generated at the radome, all the curves show similar spectra. The fuselage and wedge surfaces has the largest surfaces normal to the transverse direction, and consequently most of the transverse pressure forces are measured there.

In the streamwise direction, shown in figure 4.7(b), the picture is similar, but in this case the dominant force contributions appear at the radome and wedge surfaces. The fuselage surface is parallel to the main flow except at the downstream end of the computational domain, and hence feels a much smaller pressure force. On the other hand, the pressure forces on the fuselage dominate the vertical pressure forces, as shown in figure 4.7(c).

Because the qualitative behaviour of most of these force monitors are similar, we choose the total transverse pressure force as a representative quantity for comparison of different configurations. It should be noted that viscous forces are also acting on these surfaces, but their oscillations are negligible compared with the pressure forces.

The power spectra of the total transverse pressure forces for the original design ("Radome only") and for modification 3 are compared in figure 4.8, for speeds of 280 and 400 knots. In both cases

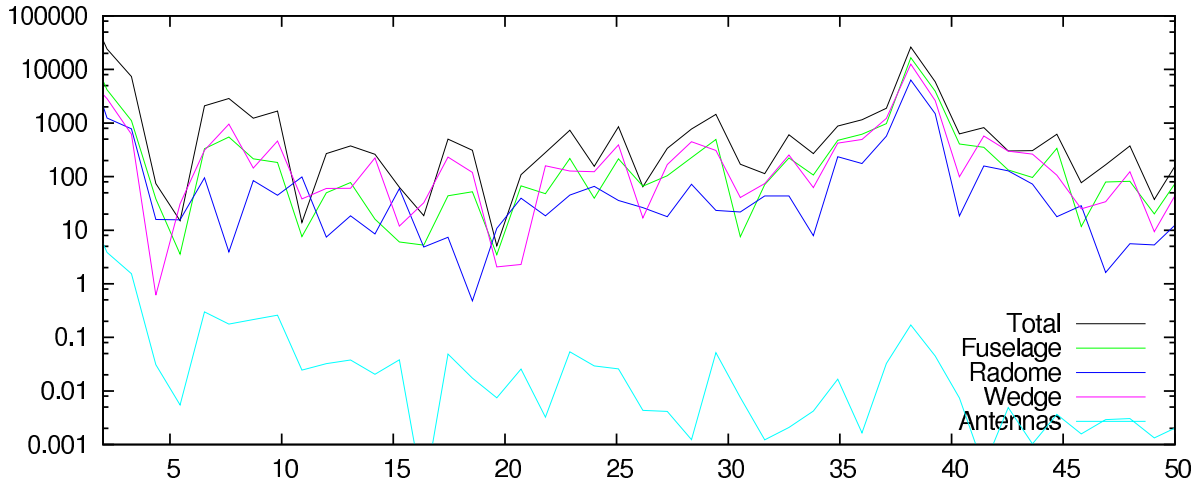

(a) Transverse pressure forces

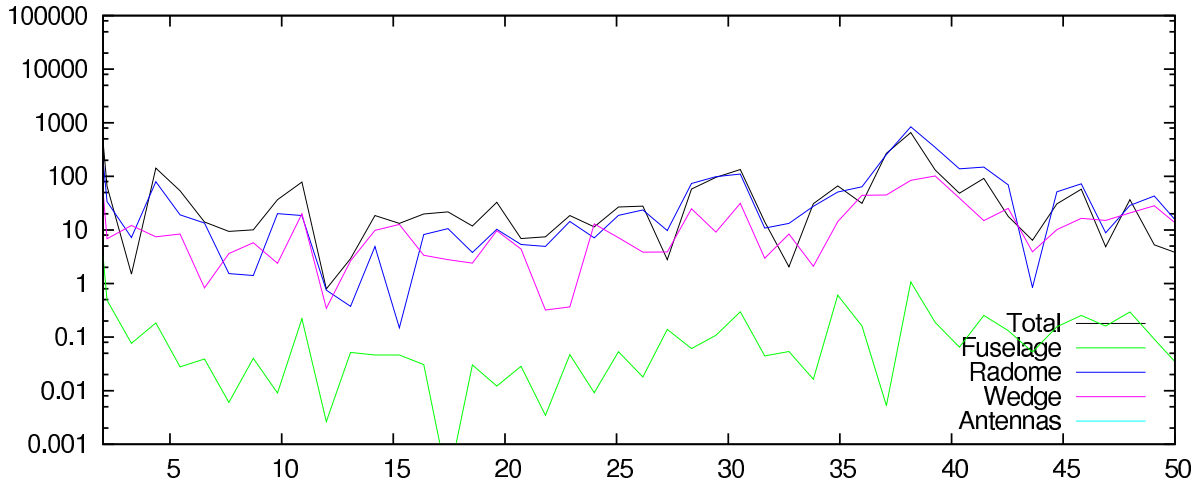

(b) Streamwise pressure forces

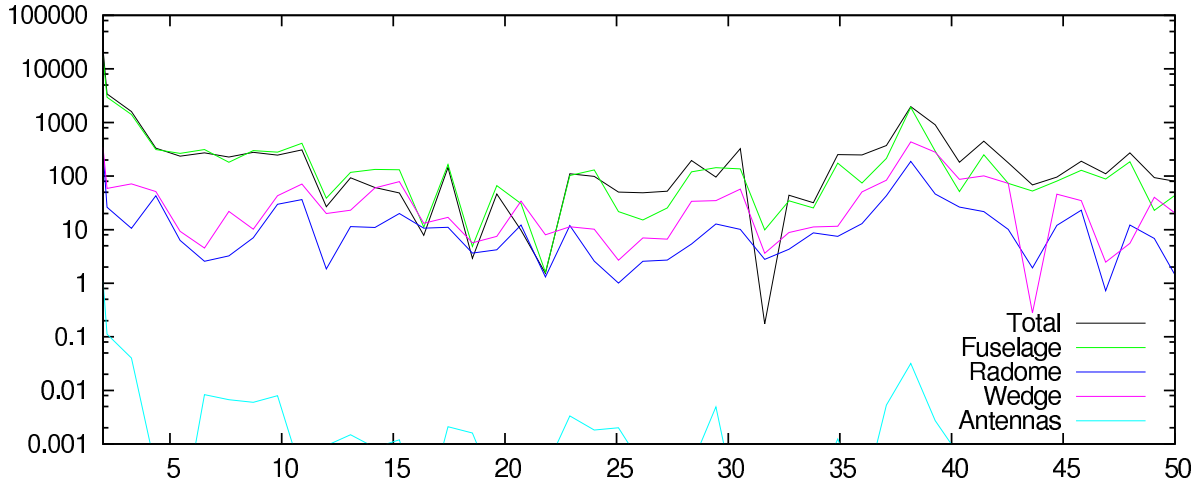

(c) Vertical pressure forces

Figure 4.7 Power spectra for pressure forces integrated over different surface parts for 280 knots with modification 3.

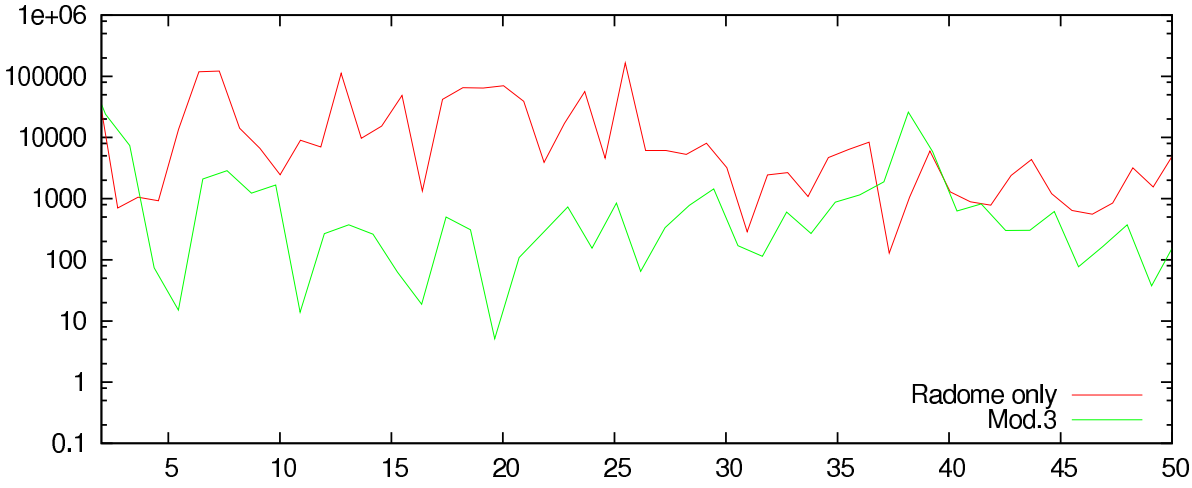

(a) 280 knots

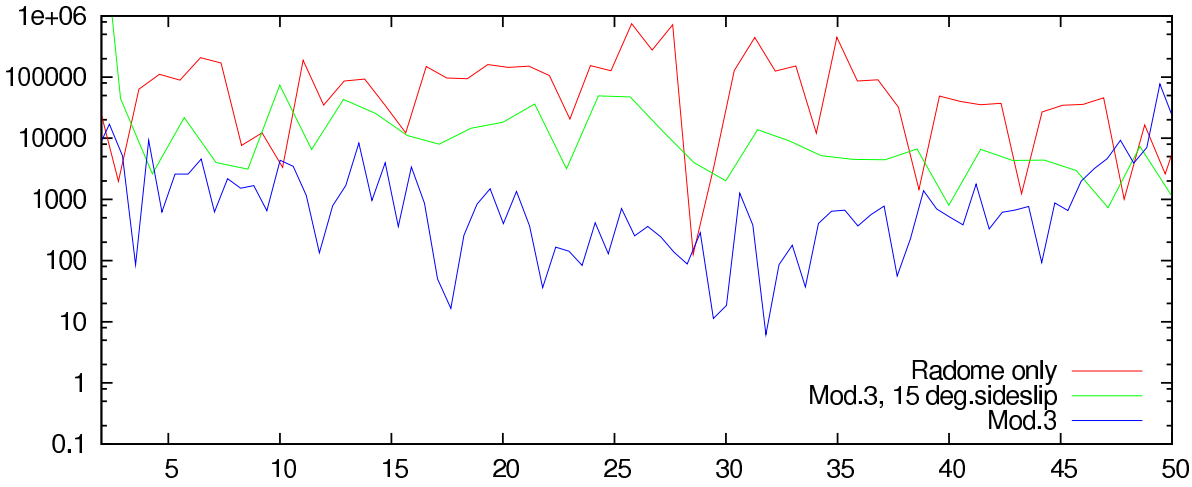

(b) 400 knots

Figure 4.8 Power spectra of total transverse pressure forces for the original design compared with modification 3.

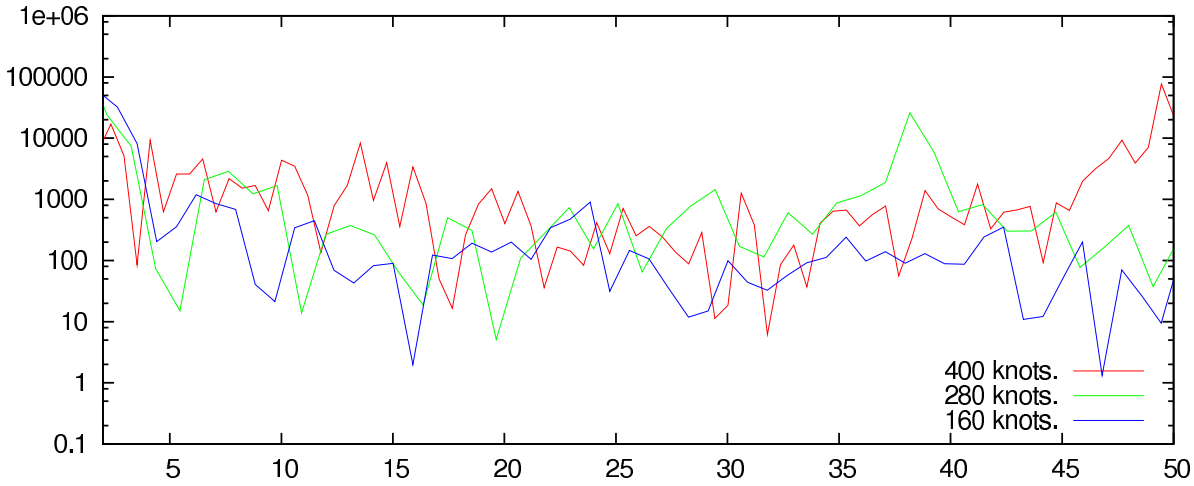

Figure 4.9 Power spectra of total transverse pressure forces for modification 3 for different speeds.

the graphs show that the power spectra are about two orders of magnitude smaller at low frequencies when the modification is included. Results from a simulation with 15° sideslip are also included in figure 4.8(b). Sideslip increases the pressure forces, but they are still smaller than for the original radome without sideslip.

Finally, we compare the power spectra of the total transverse pressure forces for three different speeds in figure 4.9. We observe that the highest amplitude above 10 Hz occurs at 49, 38 and 24 Hz for the 400, 280 and 160 knots, respectively, i.e. decreasing with speed. From figure 4.8, we see that the amplitudes for these particular frequencies are higher for the modification than for the original radome, indicating that this is related to the vortices generated by the vortex generators at the modification.

5 Conclusions

The vibration measurements show that attaching the fairing to the radome reduces, in most of the cases, the peak power in acceleration caused by the vertical and spanwise forces by up to one order of magnitude in the frequency range (0 - 25 Hz) compared with the airplane with radome only. This is consistent with the numerical simulations (which are only able to estimate the forcing caused by the turbulent motion of the wake of the radome and not the resonant response of the airplane). The observed spectrum has similar shape with maxima in the same frequencies around 4 Hz and 12 Hz, regardless of the test flight configurations. These maxima occur at the natural frequencies in the P-3C framework-system and they do not change with airspeed. We also see the propeller noise at 17 Hz and 34 Hz. The wake from the radome is broadband in nature but it triggers the 4 Hz and 12 Hz natural modes. These modes are apparent in the three cases, airplane with radome, airplane with radome and fairing and airplane with radome and pairing are dismounted (clean airplane).

The vibrations are mild for the lowest airspeeds and increase to a maximum at 360 kt. It is interesting to notice that the pilot reports a maximum in vibrations at 320 kt and a reduction beyond that airspeed. This is verified by the measurements. The vibrations in the boom though, increase with increasing airspeed and are strongest at maximum speed. The same is also the case for the vibrations in the vertical stabilizer. The magnitude of the vibrations increases with distance from CG. They have a minimum amplitude in CG, are relatively weak in cockpit but stronger in the aft part of the airplane, in empennage1 and 2, the vertical stabilizer and the boom. The strongest vibrations are measured in the aft part of the boom.

The reason for the vibrations is the excitation of the eigen-modes in the aft part of the fuselage by the broad banded turbulent wake caused by the radome. Due to limited computational resources, our computational domain is not big enough to cover the whole tail of the airplane. Although we have no simulation data in the aft part of the airplane we expect that the wake of the radome is extended to the aft part, perhaps even to the boom where it can cause the strong vibrations observed.

The topology and frequency of the wake are assessed by the simulations. They depend on the shape of the fairing. The simulations show that the fairing create a narrower and a weaker wake which reduces the transverse forces and torques at the fuselage, again resulting in a reduction of source of the vibrations. The fairing has been designed to weaken the velocity fluctuations and vortices in the wake and at the same time move the wake away from the hull.

If we assume that the aerodynamic forcing is quite white in the frequency range up to 25Hz, which they are according to the simulations, the spectrum of the measured vibrations will have peaks where the structural response of the airplane has its maxima (4Hz and 12Hz). What we measure is not the spectrum of the aerodynamic forcing, but the response of the airplane-structure to that forcing. The efficient treatment of the aerodynamic excitation of the vibrations is to design fairings that will reduce the overall turbulent noise. That can be done by weakening the vortices shed by the

radome and to move the wake away from the hull.

It is not difficult from the simulations to conclude that increasing airspeed give increased aerodynamic forces which also is observed. In the aft part of the P-3C, particularly in the aft part of the boom, the oscillations are increasing with airspeed over the entire test range. It is interesting to notice that the measured vibrations in cockpit is reduced at the highest airspeeds.

We can estimate numerically the forcing for various fairing designs. It is plausible that the fairings that give the best performance according to simulations also will give the best performance when attached to the airplane. To understand the aerodynamic consequences of the fairing, the simulations give the shape and topology of the flow field which determine how the flow field interact with the airplane. The simulations give a qualitative picture telling us whether the design will increase or decrease wake-hull interactions. The simulated power of the forcing with the radome compared to radome and fairing differs of about one magnitude at 280 kt. A difference which is close to what is observed during flight. According to the simulations, this difference increases with airspeed which is also observed in the empennage, tail and boom.

We have filtered and integrated the accelerometer signal to calculate the relative velocities and displacements for the various accelerometer positions. We tested out a 50 Hz and a 15 Hz low pass filter. The 15 Hz filter gave the best data for the study of displacement.

The displacements are highest in the empennage, tail and boom. For cases with radome without fairing, displacement amplitudes up to 10 mm are observed in the aft end of the boom. Calculation of RMS values of the sensor displacements show about the same amplitude at all weights, reduced amplitudes at maximum altitudes and enhanced vibrations for rudder doublet. The weight is of minor importance for the magnitude of the vibrations. At least in the aft part of the airplane.

At some sensor locations, for example in the cockpit, the vibrations decrease at the highest airspeeds. We can not give a physical explanation for that, but the measurements show it clearly. This is also felt by the crew. We have to mention that these effects can not be simulated by CFD methods alone, but depends on the response of the airplane frame and hull to the aerodynamic forcing provided by the surrounding vortices and turbulent boundary layer.

Most important, the RMS accelerations in the aft part of the airplane, particularly in the aft part of the boom have large amplitudes. If we compare the data for clean airplane, airplane with radome and fairing and airplane with radome, the RMS accelerations with radome and fairing is in the middle of the two others. That is a reduction in noise over background level of 50%.

In is interesting to notice that the maximum RMS of the acceleration in the high altitude test (20.000 feet) is clearly lower compared with the other tests. This proves that the vibrations are cased by aerodynamic forces since a higher altitude implies reduced air density which again implies reduced aerodynamic forces.

5.1 Further work

We have a lot of data from the accelerometers that deserves attention, but we have to limit the discussion in this report to just a few typical cases.

In the future, we would suggest that the software used to record the accelerometer data has a mechanism for marking special events like the building up of vibrations that the P-3C crew is mentioning. Then we can more easily identify and analyze the worst case events. The IMU was damaged during flight due to electrical shocks from the aircraft power supply. It would have been nice to have IMU data available for the final data analysis. Anyway, the accelerometer data is of high quality and we can derive from it interesting details about motions of various airplane sections which deviate from a straight line or even a monotonous increasing or decreasing curve. We see curves with local minima or maxima, containing modes with wavelengths shorter than the length of the airplane. The accelerometer data deserves a more careful analysis than is within the scope of this report. It should for example be made an attempt to estimate the magnitude of the errors in the derived quantities.

The fairing used under the tests was too large for operational flights, occluding the view of the instrument inside the radome. A lower fairing, but exactly shaped as the one we have tested, will probably have a smaller effect on reducing vibrations. Anyway, we have a good understanding of the mechanisms triggering the vibrations and there are several actions that can be taken. One possibility is to use a fairing that has an extended low ramp. That will modify the wake and move it away from the hull. In addition to this, stronger vortex generators added to the radome may reduce the vortex and wake behind the radome compared to the current fairing. One problem with stronger vortex generators is increased drag. A fairing built of material that is transparent to micro waves that with a droplet shape that will replace the entire radome will probably be the best solution of the problem.

To get better overview of the interactions and forces in the aft part of the P-3C, we will suggest to build a CFD model that covers the full aft part of the airplane and empennage, possibly including the slip stream of the propellers. The effects of the suggested fairings should be simulated. If they reduce the spanwise and vertical forces, we would propose to test them on the aircraft and possibly re-do the same test procedures as this report is based on.

6 ACKNOWLEDGEMENT

The authors want to acknowledge project manager Anton Vooren and test pilot Kristin Pedersen, both at Flo, and engineer Dag Jørgensen at the 333 squadron for valuable information and technical discussions.

References

[1] Øystein Lundberg. Akselerasjonsmålinger på Orion P-3C. Technical report, Forsvarets Forskningsinstitutt, 2000.

[2] Øystein Lundberg and Atle Skaugen. Nye akselerasjonsmålinger på Orion P-3C. Technical report, Forsvarets Forskningsinstitutt, 2002.

[3] Øystein Lundberg and Atle Skaugen. Vibrasjonsmålinger på Orion P-3C 3297 i forbindelse med ny ADF radar, februar 2004. Technical report, Forsvarets Forskningsinstitutt, 2004.

[4] Øystein Lundberg and Atle Skaugen. Vibrasjonsmålinger på Orion P-3C 3298 med modifisert radardome, september 2004. Technical report, Forsvarets Forskningsinstitutt, 2004.

[5] Bjørn Anders Reif and Carl Erik Wasberg. Numerical simulations of flow-induced vibrations on P-3C. Technical report, Forsvarets Forskningsinstitutt, 2003.

[6] Bjørn Anders Reif and Carl Erik Wasberg. (U) Numerical simulations of flow-induced vibrations on Orion P-3C-extended study. Technical report, Forsvarets Forskningsinstitutt, 2004.

[7] P. Spalart and S. Allmaras. A one-equation turbulence model for aerodynamic flows. *AIAA Paper*, pages 92–0439, 1992.

Appendix A Technical definitions

A.1 Flutter

Flutter involves aerodynamic forces, inertia forces and the elastic properties of a surface. The distribution of mass and stiffness in structure determine certain natural frequencies and modes of vibration. Most often the problem originates in a control surface on the aircraft. If the CG (center of gravity) for the control surface lies behind the hinge line and the control surface is displaced, and swings back towards neutral, this will cause an over swing. This can cause a divergent oscillation, increasing until the surface breaks away. The aircraft is subject to gusts and maneuver loads that can initiate this.

The fix is to place a counterweight ahead of the hinge line, or to extend the control surface forward with an inset hinge line and a built in weight in the leading edge.

Large aircraft tend to be “flabby” and have less bending and torsional stiffness. In some cases the aileron might twist the outer part of the wing instead of displacing it, causing it to move opposite to the intended direction (aileron reversal). If in this case the center of aerodynamic forces is ahead of the elastic axis and the CG behind, this will set of a divergent flutter of the wing until it breaks away. For this reason, some large aircraft have one outboard aileron near the wingtip which is in use at low speed. As speed increases this aileron is locked and the movement transferred to an inboard aileron. This is of smaller size and placed at a thicker part of wing with greater torsion stiffness. Another option is the use of spoilers which are placed closer to the main wing box, thus causing less torsion. In addition to this, some aircraft have a maximum maneuvering speed, which is the maximum speed for full control surface deflection.

A large aircraft will have all its fuel in wing tanks and as these are emptied, the CG of the wing changes both forward or aft and sometimes laterally. It is therefore important that this is done in such a way as to maintain structural stability (fuel used schedule).

A.2 Buffeting

There are two main types of buffeting, the high angle of attack and the high speed buffeting. The high angle of attack buffet is generally in conjunction with the wing stalling. As the boundary layer stagnates near the trailing edge of the wing, vortices break loose and hit the tail plane. This can be felt as a shaking and a noise in the whole plane. It is a requirement that all aircraft have a stall warning system, and by placing the tail plane in the right position this can work as a stall warning system. Otherwise, one has to have electronic devices (horns, stick pushers etc).

The other kind of buffeting, the high speed type, is generally caused by turbulence behind the shock wave on the upper surface of the wing. It can often be heard as a more staccato sound and is of a higher frequency than the low speed buffet.

Vortices will also be shed from different types of protrusions (antennas, weapons launchers etc.) and it is very important that these do not hit the vertical or horizontal stabilizer. On modern planes it has become more and more common to use vortex generators to suck up and direct this turbulence away from unwanted directions (sweepers). These can be seen on most modern aircraft. Examples are shown in figure A.1. Vortex generators are also used to insert energy into the boundary layer to delay stagnation.

The torsional and bending stiffness of the structure remains constant, the dynamic pressures increase with V^2 (V being airspeed). This is the reason why all aircraft have maximum operating speed.

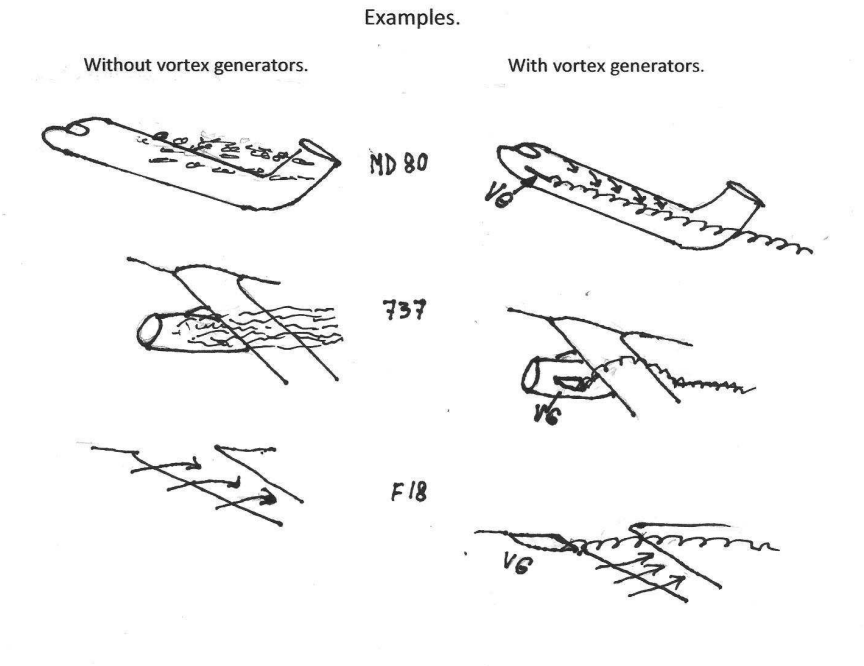

Figure A.1 Vortex generators and vortices used to enhance aircraft stability.

A.3 Methods used in the data analysis

The data are filtered using the discrete Fourier transform (DFT) method. For a discrete sample of complex data $a_0, a_1, \ldots, a_{N-1}$, where for time t_i,

$$a_i = a(t_i), \quad t = t_0, \ldots, N-1,$$

the DFT is defined as follows

$$A(\xi_k) = A_k = \sum_{n=0}^{N-1} a_n \cdot e^{i2\pi kn/N}, \tag{A.1}$$

where, $\xi_n = n/N, \quad k = 0, N-1$ and $A_0, A_{,1}, \ldots, A_{N-1}$ is a sequence of N complex numbers. Notice that $\Delta\xi = \xi_n - \xi_{n-1} = 1/N$. The original data a_n may be retrieved by the inverse transform

$$a_n = \frac{1}{N} \sum_{k=0}^{N-1} A_k e^{i2\pi kn/N}. \tag{A.2}$$

It is assumed that the data are periodic. Interesting parameters can be computed from the Fourier transform. For example the "power" spectrum

$$\mathcal{P}(k) = A_k A_k^*, \quad k = 0, \ldots, N-1,$$

where A_k^* is the complex conjugated of A_k. In the case a_i is the velocity, $\mathcal{P}(k)$ is the power at the frequency represented by k. If a_i is the acceleration $\mathcal{P}(k)$ it is not physical power, but a measure of the "amount of acceleration" at the frequency represented by k. We denote the plots of $\mathcal{P}(k)$ as power spectra.

The low pass filter is obtained by truncating certain number of elements in the spectral space before applying the inverse transform. That is

$$\hat{a}_n = \frac{1}{N} \sum_{k=0}^{M-1} A_k e^{i2\pi kn/N}, \quad \text{where} \quad n = 0, \ldots, N-1 \quad \text{and} \quad M < N-1. \tag{A.3}$$

We denote the low pass filtered data by $\hat{a_n}$. The data may be multiplied with a slowly varying periodic function to make them periodic. This may introduce some minor error in the analysis but may reduce the errors encountered when treating non-periodic data.

In our analysis, the standard deviation of the data are calculated to give a measure of the average vibrations. They are calculated according to the formula

$$a_{std} = \sqrt{\frac{1}{N} \sum_{i=0}^{N-1} (\hat{a}_i - \overline{a})^2}, \tag{A.4}$$

where

$$\overline{a} = \frac{1}{N} \sum_{i=0}^{N-1} \hat{a}_i.$$

is the average of $\hat{a}$. The root mean square of the data can be assessed through

$$a_{rms}^2 = \overline{a}^2 + a_{std}^2. \tag{A.5}$$

The low-pass filtered acceleration data has been used to calculate the relative velocities and displacements of the sensors. This information can also be used to calculate the bending of the aircraft. There is a minimum of motion in CG, see figure 3.20, therefore CG is a good choice for defining a reference frame from where the motion of the rest of the sensors can be expressed. Let the horizontal and vertical velocity be u_i, with $i = 1, 2$, the horizontal and vertical displacement be x_i. With corresponding filtered accelerations a_i we have

$$u_i(t) = u_{0i} + \int_0^t a_i(t')dt', \tag{A.6}$$

and for the displacement

$$x_i(t) = x_{0i} + \int_0^t u_i(t')dt' = x_{0i} + u_{0i}t + \int_0^t \Big(\int_0^{t'} a_i(t'')dt'' \Big) dt'. \tag{A.7}$$

We are interested in motion in the frequency range from 0 to 15 Hz. This is obtained by low-pass filtering the acceleration using a fast Fourier transform. To obtain $u_i(t)$ the acceleration is integrated. To obtain the fluctuations in $u_i(t)$ relevant for studying metal fatigue in the airplane, a running average $U_i(t)$ is computed and subtracted giving the fluctuating velocity $\delta u_i(t) = u_i(t) - U_i(t)$. This signal is then integrated to estimate 15 Hz displacement of the sensors

$$\delta x_i(t) = \int_0^t \delta u_i(t'))dt'. \tag{A.8}$$

These quantities have been calculated for each sensor giving the results shown in figure 3.20. To get even better data, the motion of CG can be subtracted from the data. In practice, the motion of CG is very steady. Many interesting parameters can be derived from the data. It is possible to calculate the standard deviation of the accelerations $s_i(a_i)$. The motion can also be decomposed into rotation about a vertical and a horizontal axis

$$\Omega_n = (\delta u_n(t) - \delta u_{cg}(t))r_n, \tag{A.9}$$

here n refers to sensor group number n.
Bending or deflection of the aircraft can also be calculated relative to CG. Assuming no deflection (stiff rotation), the displacement of each sensor location increases linearly with the distance from CG. Bending can then be calculated as a deviation from the linearity. Many of these derivations are outside the scope of this report, but the most relevant ones are summarized in section 3.

Appendix B Characteristics and positions for the various accelerometers used in the P-3C tests

The position of the accelerometers are given in meters in a reference system where the position of the airplane nose is zero.

Model	S/N	Frequency r.	Measurement r.	Sensitivity	Location	Pos.(m)	Direction
8310B25	2039445	DC-300Hz	±25g	80.30mV/g	Cockpit	7	Y
8310B25	2039446	DC-300Hz	±25g	80.90mV/g	Cockpit	7	Z
8310B25	2039447	DC-300Hz	±25g	79.60mV/g	CG	16	-Y
8310B25	2045684	DC-300Hz	±25g	80.60mV/g	CG	16	Z
8310B25	2045685	DC-300Hz	±25g	79.80mV/g	Dome	18	Y
8310B25	2045686	DC-300Hz	±25g	80.10mV/g	Empennage1	25	-Y
8310B25	2045687	DC-300Hz	±25g	79.90mV/g	Empennage1	25	Z
8310B25	2045689	DC-300Hz	±25g	79.50mV/g	Empennage2	26	-Y
8310B25	2045690	DC-300Hz	±25g	81.40mV/g	Empennage2	26	Z
8310B25	2045691	DC-300Hz	±25g	80.50mV/g	Tail	31	Y
8310B25	2045692	DC-300Hz	±25g	80.40mV/g	Boom1	35	-Y
8310B25	2045693	DC-300Hz	±25g	80.50mV/g	Boom1	35	Z
8310B25	2058327	DC-300Hz	±25g	79.50mV/g	Boom2	38	Y
8310B25	2058328	DC-300Hz	±25g	79.20mV/g	Boom2	38	Z
8310B50	2051276	DC-300Hz	±50g	39.51mV/g	Dome Fixture	18	Y

Table B.1 Accelerometer characteristics and locations.

Appendix C Modifications

Three different modifications have been considered in this study: Modification 1 (figure Appendix C.1(a)), modification 2 (figure Appendix C.1(b)), and modification 3 (figure Appendix C.1(c)).

C.1 Modification 1

The starting point for the series of investigated modifications was a configuration consisting of a backward wedge covering as much as possible space behind the radome within the given restrictions (see figure Appendix C.1(a)). Modification 1 includes a concave-shaped wedge in addition to two mounted edges on top of the bottom plate of the wedge. These two edges act as vortex generators. The main motivation for the modification is to minimize the region of flow separation downstream the radome. In addition, the vortex generators will induce vortices stabilizing the flow in the wake of the radome.

C.2 Modification 2

Modification 2 differs from the first modification in the two following ways. First, the second modification consists of a convex-shaped wedge as opposed to the concave-based design of the first modification. Second, the vortex generation edges from the first design have been replaced by a *vortex generation plate* mounted on top of the bottom part of the wedge. The vortex generation plate is depicted in figure Appendix C.1(d). The vortex generation plate includes two swept *L*-shaped leading edges which are placed on both sides of the radome.

The motivation for the above changes were to reduce separation regions occurring at both sides near the back end of the wedge for the concave configuration and to make the vortex generators less dependent on the sideslip angle. An additional important design aspect of the vortex generators were to generate a pair of vortices rotating upwards. In this way, the vortices are advected away from the fuselage.

C.3 Modification 3

In the third modification a curved fillet covering the base of the radome and wedge was added to the design (see figure Appendix C.1(c)).

The motivation for including the fillet was to reduce the separation region occurring in front of the radome (for the original configuration), to reduce the strength of the vorticity structures generated from this region, and to move these structures away from the fuselage.

h

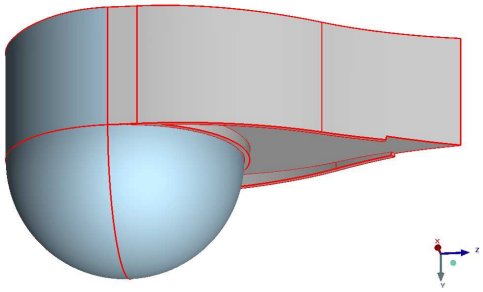

(a) Modification 1

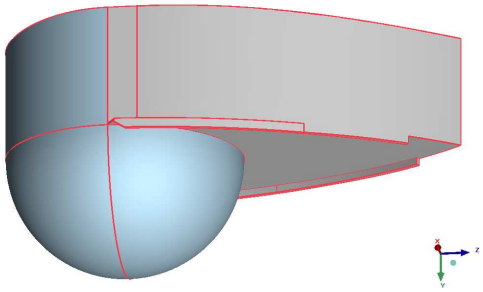

(b) Modification 2

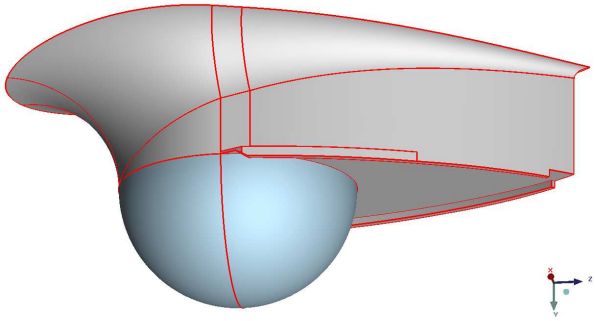

(c) Modification 3

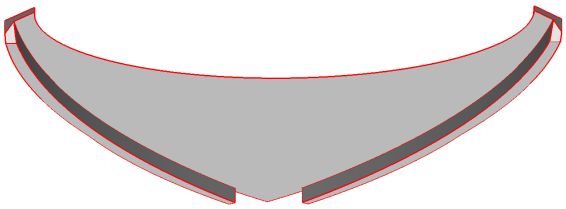

(d) Vortex generation plate (Mod. 2 and Mod. 3)

Figure C.1 Modifications.

Appendix D Numerical simulation mesh

	Fuselage (centre)	Fuselage (sides)	Radome (incl. front fillet)	Modification (flat plate and vortex gen.)	Modification (sides)	Antennas
Max. size	8 mm	16 mm	8 mm	4 mm	8 mm	4 mm
Prism layers	6	6	5	0	5	0

Table D.1 Maximum cell side sizes and number of prism layers at different surfaces.

The mesh used for the simulations is made up by tetrahedral cells, with prism cells used to make the thinnest cells close to the surfaces. The mesh is generated by the meshing program ICEM CFD from Ansys Inc. Maximum side sizes for the mesh cells at different parts of the geometry are given in table D.1. The prism layers have a minimum thickness of 1 mm and a growth rate of 1.5 for each layer. The global maximum cell side size is 128 mm.

In terms of the scaled "wall unit" y^+, defined using the friction velocity $u_\star$ and the kinematic viscosity ν as $y^+ = yu_\star/\nu$, the minimum cell thickness of 1 mm in the prism layer corresponds to $y^+ \sim 150$ for 280 knots. To simulate the boundary layer without resorting to the RANS model for turbulence, this cell thickness would have had to be a factor 100 smaller.

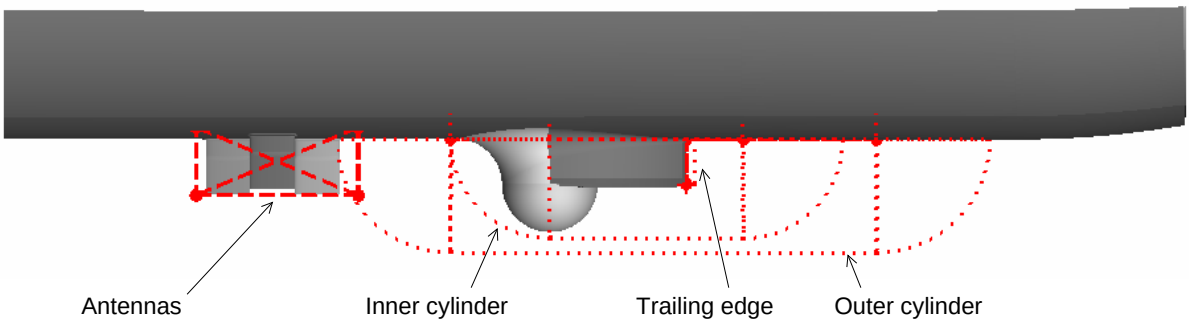

Figure D.1 Density regions where the maximum mesh cell size is limited.

	Maximum cell side size	Number of cells	Radius
Antennas	32 mm	N/A	N/A
Inner cylinder	16 mm	42	0.672 m
Outer cylinder	32 mm	24	0.768 m
Trailing edge	8 mm	7	0.056 m

Table D.2 Parameters for the mesh density regions.

In addition, four density regions are defined, with corresponding maximum mesh cell sizes. One region contains the antennas upstream the radome, two rounded cylinders cover the radome and

modifications, and a small rounded cylinder is placed at the trailing edge of the modification. The density regions are shown in figure D.1, and their parameters are given in table D.2.

The final mesh size is between 15 and 20 million cells for the geometries considered. Close-up of the surface mesh at the radome and modfication 3 are shown in figure D.2, and the mesh in the symmetry plane around the radome is shown in figure D.3.

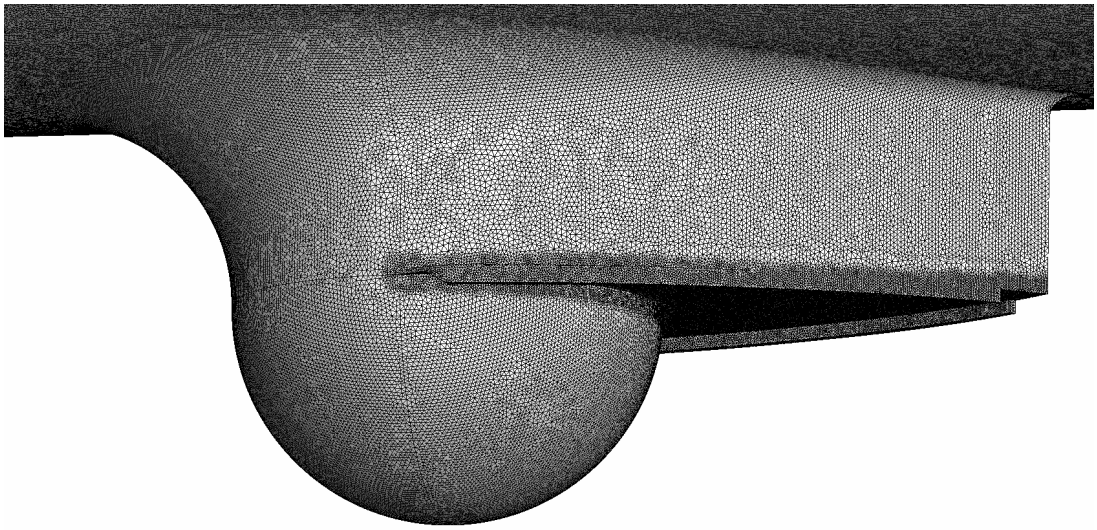

Figure D.2 Surface mesh at the radome and modification 3.

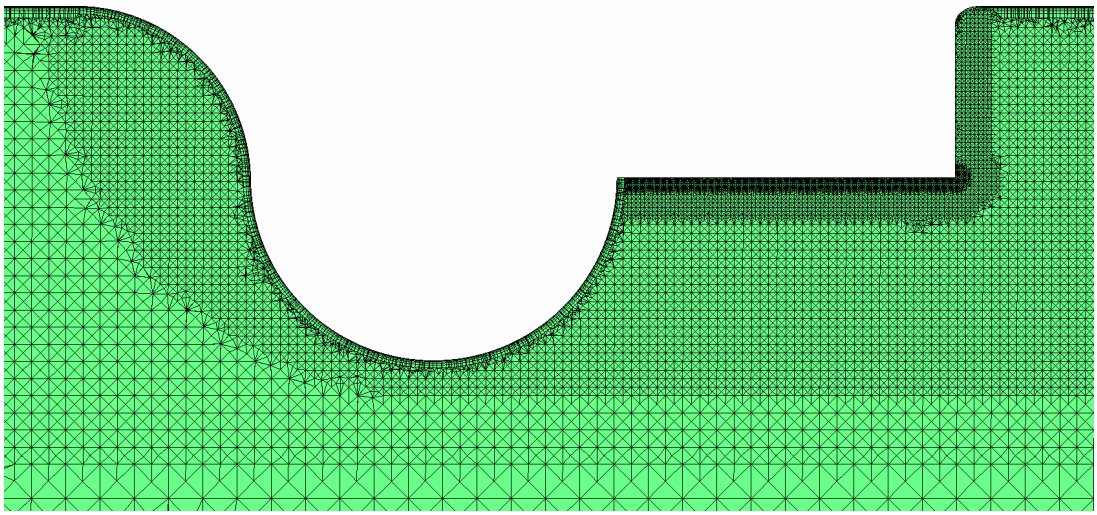

Figure D.3 Volume mesh in the symmetry plane close to the radome.